Key Points:

- Idealized simulations of moist Kelvin waves and the Madden-Julian Oscillation (MJO) are found to depend critically on the structure of the background zonal flow
- The reason stems partly from changes in the Rossby wave critical line that affect the lateral forcing of the tropics by midlatitude eddies
- A second pathway is through mediation of multi-scale interactions internal to the tropics that appear to govern the simulated MJO

Correspondence to:

S. N. Tulich,
stefan.tulich@noaa.gov

On the Regionality of Moist Kelvin Waves and the MJO: The Critical Role of the Background Zonal Flow

S. N. Tulich[1,2] and **G. N. Kiladis[2]**

[1]CIRES, University of Colorado Boulder, Boulder, CO, USA, [2]NOAA Physical Sciences Laboratory, Boulder, CO, USA

Abstract A global model with superparameterized physics is used to shed light on the observed regionality of convectively coupled Kelvin waves and the Madden-Julian Oscillation (MJO). A series of aquaplanet simulations over zonally uniform sea-surface temperatures is performed, in which the axisymmetric structure of the background zonal flow $[\bar{u}]$ is altered through nudging, while maintaining a quasi-fixed rainfall climatology. Results show that nudging $[\bar{u}]$ at the equator to match profiles typical of the Indo-Pacific or eastern Pacific sectors yields eastward-moving tropical rain spectra typical of those sectors. Two different mechanistic pathways are identified as being responsible for this mean-flow dependence, in addition to Doppler shifting effects. The first is through shifts of the Rossby wave critical line in the subtropical upper troposphere that affect the lateral forcing of Kelvin-mode circulations at the equator by eastward and equatorward-propagating eddies impinging on the tropics from higher latitudes. The second is through changes in the strength of the mean cyclonic shear in the lower tropical troposphere that affect the degree to which intraseasonal fluctuations in Kelvin-mode zonal winds modulate the activity of higher-frequency equatorial Rossby-type eddies. In cases where the mean low-level cyclonic shear is enhanced, the strength of this modulation, referred to as "shear-induced eddy modulation" or SIEM, is also seen to be enhanced, such that MJO-like modes of variability are rendered either unstable or near neutral, depending on the strength of the shear.

Plain Language Summary The climatological behavior and character of large-scale weather patterns in the tropics is known to depend strongly on geographic location, but for reasons that remain poorly understood. Here this problem is addressed in the context of two important types of weather patterns that preferentially move eastward and have spatial scales ranging from thousands to even tens of thousands of kilometers. A sophisticated model of the global atmosphere is used to show that regional variations of the prevailing or "background" zonal wind are of leading importance, for at least two reasons. The first involves the effects of the background zonal wind on the ability of eastward-moving weather patterns in the midlatitudes to remotely excite eastward-moving weather patterns in the tropics. The second involves the effects of the background zonal wind on the nature of interactions between different scales of motion internal to the tropics, which can ultimately give rise to a special kind of slow-moving weather pattern, whose spatial scale is comparable to the size of the planet.

1. Introduction

The tropics are home to a myriad of zonally propagating wavelike disturbances in both cloudiness and circulation (Kiladis et al., 2009, and the references therein). These "convectively coupled" waves include a variety of different types, all of which exhibit some degree of regionality, in terms of their average amplitude and speed of propagation. A relevant example is the Madden-Julian Oscillation (MJO), whose relatively slow eastward propagation at ~5 m s^{-1} tends to be most pronounced in terms of cloudiness and precipitation over the Indo-Pacific warm pool region between 60° and 150°E. Outside of this region, the disturbance behaves more like a "dry" or weakly coupled phenomenon, with a faster eastward propagation speed of anywhere between 10 and 30 m s^{-1} (Adames & Wallace, 2014a; Hendon & Salby, 1994; Knutson & Weickmann, 1987; Straub, 2013). Convectively coupled Kelvin waves (hereafter, simply Kelvin waves) are another class of eastward-moving disturbances that generally propagate more slowly over the Indo-Pacific warm pool region as compared to the rest of the tropics (i.e., 7–14 vs. 15–20 m s^{-1}; Roundy, 2008, 2012; Straub & Kiladis, 2002; Yang et al., 2007). Unlike the MJO, however, Kelvin waves are generally most active, in terms of filtered OLR variance, over the central and eastern tropical Pacific between 160° and 260°E (Kiladis et al., 2009;
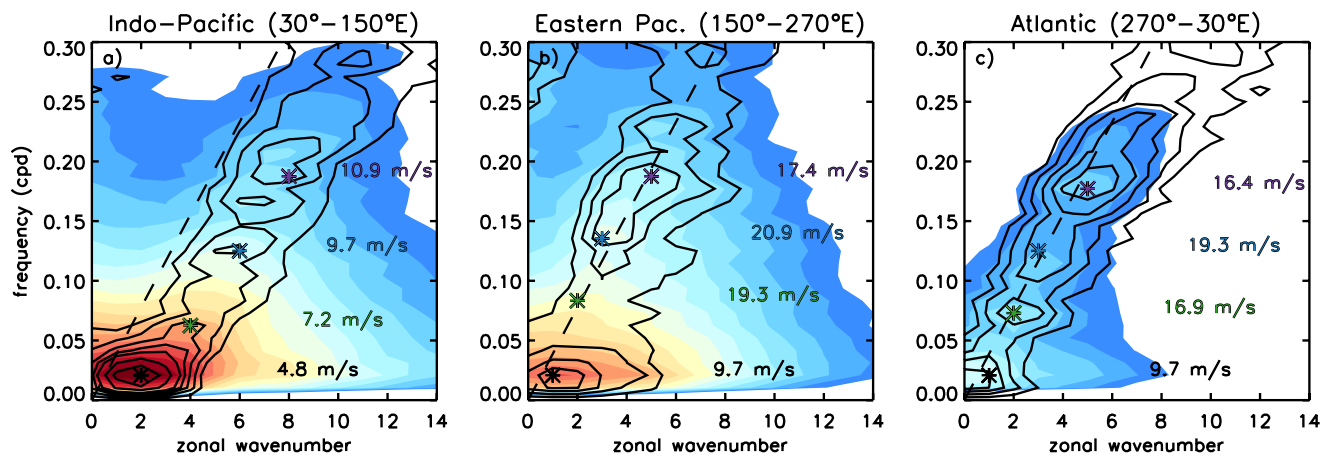
Figure 1. Regional space-time spectra of TRMM 3B42 rainfall (Huffman et al., 2007) for three different sectors of the tropics between 15°S–15°N: (a) "Indo-Pacific" (30°E–150°E), (b) "East Pacific" (150°E–270°E), and (c) "Atlantic" (270°E–30°E). Shading denotes the raw variance, with logarithmic intervals starting at 1×10^{-2} mm^2 day^{-2}. Contours denote where the ratio of the raw variance to a smoothed "red-noise" background exceeds 1.1, with intervals of 0.1 up to 1.5 and 0.2 thereafter. Colored symbols with text denote the locations and corresponding phase speeds of various local maxima in the signal-to-noise ratio. Sloping dashed line denotes an eastward phase speed of 18 m s^{-1}. For ease of visualization, only zonal wavenumbers 0–14 and frequencies ≤0.3 cpd are shown. The spectra were calculated following the approach outlined in Dias and Kiladis (2014), except for the use of a broader tapering window: 144° in longitude and 96 days in time. The functional form of the tapering window is the same as described in Wheeler and Kiladis (1999). Background spectra were estimated separately for each sector, using the smoothing procedure of Tulich and Kiladis (2012).

Roundy, 2008). While studies aimed at explaining these sorts of regional variations in tropical wave activity and propagation speed have typically appealed to some aspect of the basic state (e.g., Das et al., 2016; Dias & Kiladis, 2014; Kang et al., 2013; Wang & Chen, 2017), there is generally no consensus as to which aspects of the basic state are most important or why, and the problem remains open.

To more objectively quantify the regionality of Kelvin waves and the MJO, Figure 1 compares the climatological (all-season) space-time spectra of TRMM 3B42 rainfall for three different sectors of the tropics: (a) "Indo-Pacific" (30°E–150°E), (b) "Eastern Pacific" (150°E–270°E), and (c) "Atlantic" (270°E–30°E). Details about the methods used to obtain these regional spectra can be found in the figure caption. Each spectrum shows clear evidence of both Kelvin waves and the MJO, where the Kelvin waves can be identified as a broad lobe of enhanced power at periods less than 20 days, extending upwards and to the right, away from the signals of the lower-frequency MJO. In both the Eastern Pacific and Atlantic spectra, the orientation of the Kelvin lobe is such that the signals are nearly non-dispersive, with zonal phase speed largely independent of zonal wavenumber k, in accordance with linear equatorial wave theory. The story is quite different in the Indo-Pacific spectrum, however, where the Kelvin lobe is shifted to the right of its typical position, such that larger wavenumbers propagate significantly faster than smaller wavenumbers. For example, at $k = 8$, the strongest wave signals have zonal phase speeds of around 11 m s^{-1}, compared to just 7 m s^{-1} at $k = 4$. The implied group velocity associated with the change in phase speed is estimated to be around 15 m s^{-1}. Though not as evident in the *global* space-time spectrum of tropical convection (see Figure 1 of Kiladis et al., 2009), this non-classical dispersion is a well-known signature of extratropical storm track disturbances, as seen in global spectra of horizontal winds in the subtropics and higher latitudes (Adames et al., 2014; Gehne & Kleeman, 2012; Hayashi & Golder, 1977; Hoskins & Yang, 2000; Lee & Held, 1993; Pratt, 1977; Yang & Hoskins, 2016). Might there be an extratropical forced class of dispersive, slow-moving Kelvin-like disturbances at low latitudes over the Indo-Pacific (rather than a "continuum" of MJO variability, as suggested in Roundy, 2012)? Addressing this question, in addition to explaining why the convective signals of the MJO are so much stronger over the Indo-Pacific as compared to the rest of the tropics, is the primary objective of this study.

To untangle cause and effect, numerical models can be used to investigate how the basic state affects the character of large-scale tropical variability. Along these lines, Kang et al. (2013) employed a relatively coarse-resolution global atmosphere model with a mass-flux-based convection scheme to study how the distribution of sea-surface temperature (SST) affects the simulated space-time spectrum of tropical low-level

zonal winds. To simplify the problem, they assumed a completely water-covered Earth (i.e., an "aqua-planet") with a zonally uniform SST distribution. Their results showed a strong sensitivity of MJO-like variability in the model to the degree of meridional curvature in the SST profile (see also Jiang et al., 2020; Wang et al., 2018), in addition to whether the profile was maximized or off the equator. Using a very similar model, however, Sooraj et al. (2009) found that the simulated spectrum of tropical variability was strongly sensitive to the vertical structure of the basic state zonal wind near the equator, even in the absence of changes to the underlying SST distribution. In particular, those authors reported an enhancement in eastward-moving intraseasonal zonal wind variability at planetary zonal wavenumbers (k = 1–4) when background low-level westerlies beneath upper-level easterlies (like what is observed over the Indo-Pacific) were imposed over a limited portion of the model domain. While the mechanisms responsible for this enhancement were not addressed, evidence was given to suggest an important role of the vertical and/or meridional shear of the background zonal wind.

A physical basis for suspecting that mean-state shear might be critical to the MJO can be found in previous studies that have pointed to interactions between the disturbance's circulation and higher-frequency Rossby-type eddies as being of central importance to its propagation (Andersen & Kuang, 2012; Chikira, 2014; Kiranmayi & Maloney, 2011; Maloney, 2009; Wolding et al., 2016). The reason stems from the nature of these interactions, which leads to the eddies being relatively more active (and hence, more effective at causing lateral mixing of dry air from the subtropics into the tropics) to the west of the MJO's convective envelope, as compared to further east. In theoretical studies that have sought to account for this effect, the approach has been to essentially assume a linear relationship of the form:

$$S' = \gamma u'_e, \tag{1}$$

where primes denote perturbations on intraseasonal time scales, S' is a bulk measure of the anomalous eddy activity, u'_e is a bulk measure of the anomalous low-level zonal wind in the vicinity of the equator, and γ is a positive scaling coefficient (Adames & Kim, 2015; Sobel & Maloney, 2013). The rationale stems from observational and modeling work showing that periods of anomalous MJO westerlies tend to be characterized by enhanced mean cyclonic shear and barotropic energy conversion, while the opposite holds true during periods of anomalous MJO easterlies (Andersen & Kuang, 2012; Maloney & Dickinson, 2003). However, in a more recent observational study of the MJO during boreal winter, Wang et al. (2019) obtained evidence that the strength of this modulation, referred to as "shear-induced eddy modulation" (SIEM), is governed in part by the strength of the background cyclonic shear in which the MJO is embedded, owing to the effects of a non-linear eddy-eddy interaction term.

The past several decades have seen considerable progress in our ability to simulate moist tropical waves, without having to rely on problematic convection schemes (Chao & Lin, 1994; Lee; et al., 2003; Maloney & Hartmann, 2001). Through recent advances in computing power, it is now possible to run global models at horizontal grid spacings fine enough to at least partially resolve the circulations of deep convective cloud systems (Stevens et al., 2019; Wedi et al., 2020). Such high-resolution models, however, remain computationally quite expensive and thus, are not yet practical for highly repetitive/iterative hypothesis testing. As an alternative (Grabowski & Smolarkiewicz, 1999), devised an intermediate approach that has come to be known as "superparameterization" (SP). The idea is to embed a cyclic, two-dimensional cloud-resolving model (2-D CRM) inside each grid box of a relatively coarse-resolution global model. Improved simulation of moist tropical variability, including the MJO, has been a consistent finding in studies comparing SP models to their conventional counterparts (e.g., Hannah et al., 2020; Randall et al., 2003; Tao et al., 2009). This improved simulation has prompted a growing number of authors to adopt such models as tools for studying the origin and dynamics of large-scale tropical wave phenomena (e.g., Andersen & Kuang, 2012; Arnold et al., 2013; Benedict & Randall, 2011; DeMott et al., 2013; Grabowski, 2003; Ma & Kuang, 2016; Pritchard et al., 2014).

In this study, a global model with SP physics is used to explore the hypothesis that much of the observed regionality of Kelvin waves and the MJO can be attributed to regional variations in the background zonal flow, owing to mediation of both tropical-extratropical interactions and convection-wave interactions internal to the tropics. The approach is to perform a series of idealized aquaplanet simulations over zonally uniform SSTs, in which the axisymmetric structure of background zonal flow is altered through nudging. Because only the zonal-mean part of the flow is affected, complications that arise due to introducing zonally

asymmetric perturbations are avoided. In particular, the approach taken here is designed to ensure the model's simulated rain climatology remains close to that obtained in a free-running "control" integration, enabling isolation of the effects of the background zonal flow.

The next section describes the experimental approach, including the SP model and nudging methodology. Section 3 then describes an analysis of tropical-extratropical interactions in the context of the control integration. This analysis sets the stage for Section 4, which documents a strong sensitivity of the model's eastward-moving tropical spectrum to both the vertical and meridional structures of the background zonal wind. Further tests are described in Section 5, where the mean-flow dependence of the model is studied under eddy damping of the midlatitudes. Section 6 provides a summary and some concluding remarks.

2. Experimental Approach

2.1. Model Description and Control Simulation

The model is the global SP version of the Weather Research and Forecast model (SP-WRF). A detailed description of the SP-WRF can be found in Tulich (2015), hereafter T15. Briefly, a 2-D CRM version of the standard WRF is embedded inside a 3-D global version of the same model. This seamless coupling is unlike that of most other SP formulations, where models with different vertical grids and dynamical approximations are stitched together. The model includes the effects of convective momentum transport, using a novel scalar-based approach. As shown in T15, the SP-WRF is capable of producing realistic simulations of weather and climate with fidelity comparable to that of other current state-of-the-art global models (see also Figures A1–A3)

To provide a baseline for comparison, the SP-WRF is first used to perform a 6-year aquaplanet simulation under zonally uniform SSTs and perpetual equinox conditions. The SST profile is chosen to crudely match observations, using an analytic form designed to ensure a symmetric but otherwise realistic decay with latitude about an equatorial maximum of 28°C (see Figure 2a). The global model grid spacing is $2.8° \times 2.8°$ in the horizontal, with 51 vertical levels stretching from the surface to a height of roughly 27 km; the embedded CRMs each have 32 columns with 4-km horizontal grid spacing. The effects of unresolved physics on the CRM grid are handled using the same set of schemes as in T15, except for radiation effects, which are now handled using the Rapid Radiative Transfer Model for GCMs (RRTMG; Iacono et al., 2008). Also, rather than depending on the large-scale flow, the CRM orientation is now treated stochastically, so that no horizontal direction is statistically preferred over any other (see Appendix A for further details).

The model behavior in the above setup, defined as the "control," is found to be broadly realistic. As shown in Figure 2b, for example, the simulated time- and zonal-mean surface rain is similar to that seen on Earth, with a relatively narrow band of intense rain centered at the equator and broader belts of more moderate rain at higher latitudes, reflecting the model's midlatitude storm tracks. The background zonal winds, as shown in Figure 2c, are easterly throughout the depth of the tropical troposphere (with the largest values near the surface), while westerlies prevail at higher latitudes, in association with a pair of well defined subtropical and eddy-driven jets, centered at around 25° and 50° latitude, respectively. The average space-time spectrum of tropical rain (Figure 2d) shows evidence of both westward-moving equatorial Rossby-type waves and eastward-moving Kelvin-type waves. The latter are by far the most dominant, however, and exhibit the same sort of non-classical dispersion as seen in the observed Indo-Pacific spectrum of Figure 1a. In Section 3, evidence is given to suggest that this non-classical dispersion is almost certainly a result of external forcing of the tropics by eddies at higher latitudes.

2.2. Method for Altering the Background Zonal Flow

To examine how the above spectrum is affected by changes in the background zonal flow, a very strong nudging term is added to the right hand side of the model's prognostic zonal momentum equation, that is,

$$\frac{\partial \rho u}{\partial t} = \ldots + [\rho] W_T \frac{(U_T - [u])}{\tau}, \tag{2}$$

where ρ is the model's density variable, $[\cdot]$ denotes a zonal average, U_T is a "target" zonal wind profile (discussed further below), τ is the nudging time scale (set to 1 h), and W_T is a latitude-dependent and
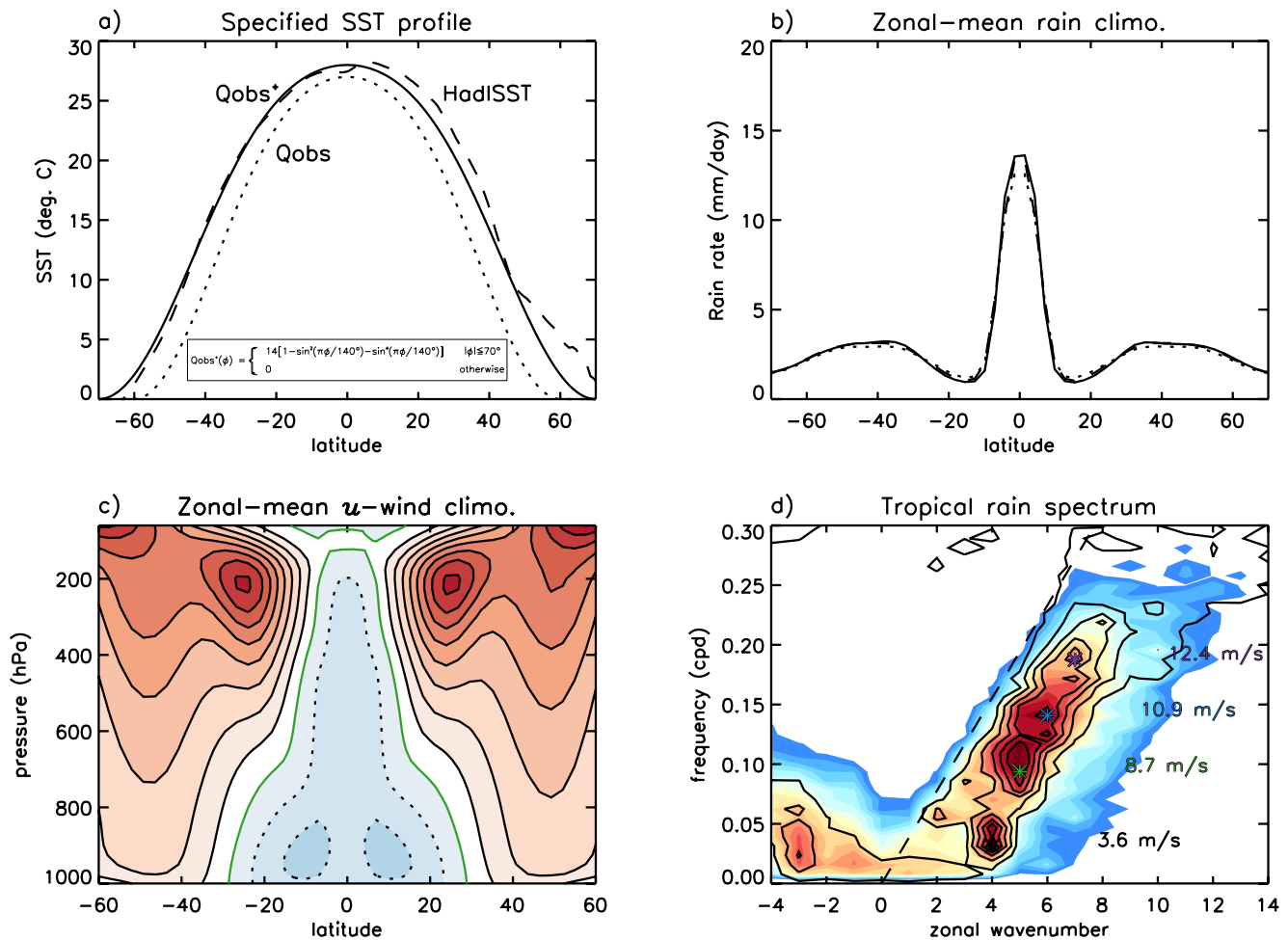
Figure 2. Select results from the 6-year control aquaplanet simulation. (a) Specified SST profile (denoted Qobs$^+$; solid), as compared to the original Qobs profile (dotted) of Neale and Hoskins (2000), as well as the 1979–2012 climatological zonal-mean of observed HadISST data (Rayner et al., 2003, dashed); inset shows the functional form of Qobs$^+$, where ϕ is latitude. (b) and (c) Time-mean and zonal-mean simulated rain profile (solid) and zonal wind distribution, respectively; dashed and dotted curves in panel (b) are for sensitivity runs in which the model's zonal-mean zonal wind is altered through nudging (see text for details); contour intervals in panel (c) are 5 m s^{-1}, with negative values dashed and the zero level shown in green. (d) Similar to Figure 1, but for the global (as opposed to regional) space-time spectrum of the simulated tropical rain, where contour levels for the signal-to-noise ratio start at 1.2 with uniform intervals of 0.7.

height-dependent weighting function. The latter is chosen so that nudging is only applied at model levels below 75 hPa, with amplitude decaying as cosine squared in the meridional direction, from a value of one at the equator to zero poleward of 5° latitude. To mitigate the effects of this nudging on other aspects of the simulated climate (via Coriolis effects, symmetric instabilities, etc.), a similar nudging term is added to the meridional momentum equation. The form of the nudging in this case is given by:

$$\frac{\partial \rho v}{\partial t} = \ldots + [\rho]\frac{(v_c - [v])}{\tau}, \tag{3}$$

where v_c is the time-mean and zonal-mean meridional wind field taken from the control simulation (i.e., v_c is a function of both latitude and height). As demonstrated by the almost perfect overlap between the dashed and solid curves in Figure 2b, inclusion of the latter strong nudging of zonal-mean divergence serves to prevent any significant drift in the simulated time-mean and zonal-mean rain profile. Similar statements hold true for the simulated time-mean and zonal-mean moisture and temperature fields (see Figure S1). Any systematic change in the model's tropical wave spectrum can thus be attributed solely to the nudging of the background zonal flow. The choice of nudging time scale τ is critical in this regard: adopting values of $\tau > 1$ h are found to be increasingly less effective at preventing the simulated time-mean rain pattern from drifting away from that of the control integration.
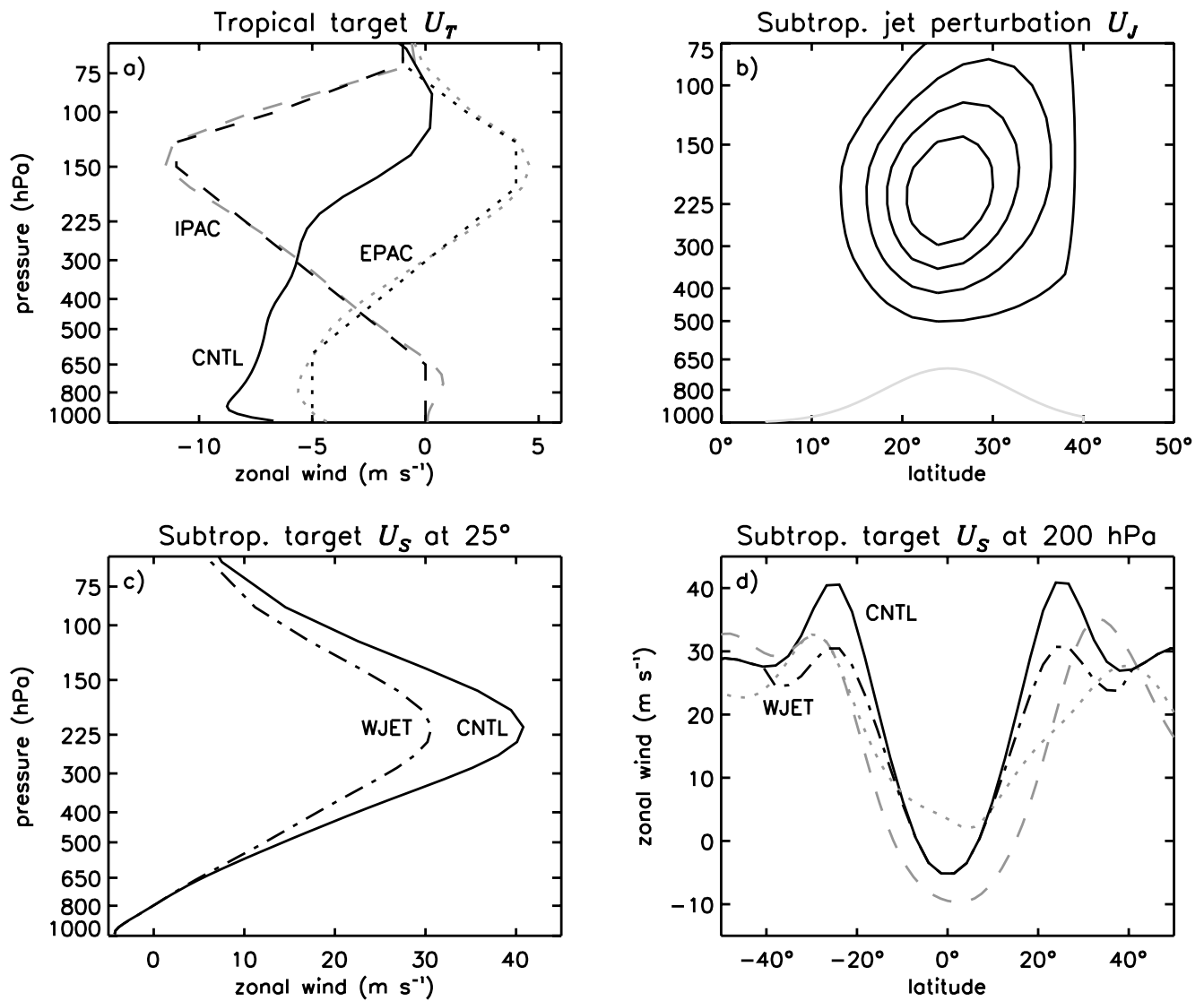
Figure 3. (a) Target equatorial zonal wind profiles (U_T) for the nudged IPAC and EPAC cases (dashed vs. dotted black, respectively), as compared to observed annual-mean and zonal-mean climatological profiles for these two respective sectors, averaged between 5°S and 5°N (dashed vs. dotted gray, respectively); solid curve is similar but for the zonal-mean climatological profile in the control run (CNTL). (b) Subtropical jet perturbation pattern U_j with contour intervals of 2 m s^{-1} and the zero contour omitted; the gray curve at bottom denotes the meridional form of W_S (see text for details). (c) Vertical structure of the target subtropical zonal wind field U_S at 25° latitude (dot-dashed; denoted WJET), as compared to the climatological profile in CNTL (solid). (d) Similar to panel (c) but for the meridional structure of the WJET profile at 200 hPa, together with observed annual-mean and zonal-mean profiles for the IPAC and EPAC sectors (gray dashed and dotted curves, respectively).

Two different target zonal wind profiles (U_T) are considered in this study, as indicated in Figure 3a. The first (denoted IPAC; dashed) is representative of observed annual-mean conditions over the Indo-Pacific sector (estimated using ERA-Interim data for the period 1979–2013; Dee et al., 2011), with relatively strong upper-level easterlies over nominal low-level westerlies (approximated by $U_T = 0$ below 650 hPa). The second (denoted EPAC; dotted) is representative of observed annual-mean conditions over the East Pacific sector, with more moderate upper-level westerlies over comparable low-level easterlies. These profiles stand in contrast to the more vertically uniform background easterly flow, albeit with modest westerly shear, typical of the non-nudged control simulation (denoted CNTL; solid black). Note that because the nudging of [u] is applied only near the equator, the net effect is to alter both vertical and meridional structures of the background zonal flow in the tropics and subtropics, as shown later in Figures 9c and 10a.

Besides these near-equatorial changes in the background zonal flow, this study also seeks to quantify the effects of changes in the strength of the climatological subtropical westerly jet. The motivation stems from previous studies showing synoptic-scale Rossby wave trains propagating eastward and equatorward in the subtropics as being potentially important driving agents of Kelvin waves (Huaman et al., 2020; Roundy, 2014; Straub & Kiladis, 2003a) and the MJO (Hall et al., 2017; Hsu et al., 1990; Lin et al., 2009; Matthews & Kiladis, 1999; Ray & Zhang, 2010). Because such eastward-moving wave trains depend crucially on the presence of background westerlies (Yang & Hoskins, 1996), any change in the strength of the subtropical westerly jet will almost certainly affect their ability to potentially modulate eastward-moving convection variability in the tropics.

To explore this idea, a second nudging term is added to the right side of the model's zonal momentum equation, that is,

$$\frac{\partial \rho u}{\partial t} = \ldots + [\rho] W_S \frac{(U_S - [u])}{\tau}, \tag{4}$$

where τ is set to 6 h in this case, U_S is a specified latitude-dependent and height-dependent target zonal wind field, and W_S is a weighting function similar to W_T but with meridional form given by the gray curve in Figure 3b. The form of U_S is symmetric about the equator and is defined as:

$$U_S \equiv u_c - U_j, \tag{5}$$

where u_c is the simulated time-mean and zonal-mean zonal wind in the control simulation and U_j is a positive-definite perturbation pattern, chosen to produce a subtropical jet whose peak wind speed is 25% weaker than in the control simulation (denoted WJET; see Figures 3b and 3c). As shown in Figure 3d, motivation for restricting the analysis to the case of jet weakening stems from the fact that the mean jet produced in the control setup is already too strong in comparison to observed annual-mean and zonal-mean conditions for either of the two regional sectors of interest, although jets of this magnitude are often present during individual seasons, especially in the IPAC sector (observations not shown).

In summary, two types of nudged simulations are considered herein: one in which the nudging is applied exclusively in the deep tropics, and the other in which nudging is also applied in the subtropics, to reduce the strength of the subtropical jet. The former are later referred to as "standard," while the latter are referred to as "weak jet" (WJET). It should be noted that because the climatological rain distribution tends to drift more strongly away from that of the control in the weak-jet simulations, the time scale of the meridional wind nudging in Equation 3 is reduced in these runs from 1 h to 10 min. As illustrated by the dotted curve in Figure 2b, this choice yields a rain climatology that is reasonably close to that of the control, with differences of around 10% near the equator. For future reference, Table 1 contains a list and brief descriptions of the various aquaplanet simulations documented in this study.

3. Extratropical Variability and Forcing in the Control Simulation

Before considering how the model responds to changes in the background zonal flow, this section describes a comprehensive analysis of extratropical variability and its forcing of the tropics in the control simulation. Results for the northern and southern hemispheres are combined on the basis of the configuration's symmetry. The starting point of the discussion is the space-time spectrum of the vertical component of the vorticity field at 200 hPa (ζ200) in the extratropics. The intent is to show how the non-classical dispersion of the simulated Kelvin waves is virtually identical to that of eddies in the model's midlatitude storm tracks, whose signals can be understood using linear Rossby wave theory. Attention is then turned to the composite horizontal structures of the simulated Kelvin waves, which provide clear evidence of remote eddy forcing from the midlatitudes. The proposed mechanism of the forcing is described thereafter, along with an assessment of its energetic importance, relative to convective heating internal to the tropics. The diagnostics introduced in this section are used further in Sections 4 and 5.

3.1. Spectral Analysis of ζ200 in the Extratropics

Figure 4 shows the climatological spectra of ζ200 for two different latitude bands in the extratropics, one encompassing the model's time-mean eddy-driven jet between 45° and 55° and the other encompassing its

Table 1
List and Brief Descriptions of the Various Superparameterization-Weather Research and Forecast Model Aquaplanet Simulations Documented in This Study

Simulation name	Brief description
Control (CNTL)	Free-running integration under perpetual equinox conditions, with SST profile given by the analytical Qobs* profile (solid curve) in Figure 2a
Standard IPAC/EPAC	Zonal-mean zonal wind [u] in the deep tropics nudged to the IPAC/EPAC profile (black dashed/dotted in Figure 3a); zonal-mean meridional wind [v] nudged at all levels and latitudes to the time-mean and zonal-mean distribution obtained in CNTL
Weak-jet IPAC/EPAC	Similar to the standard IPAC/EPAC case, but with additional nudging of [u] applied in the subtropics to reduce the peak strength of the simulated time-mean and zonal-mean subtropical jet by 25% in both the northern and southern hemispheres
No-shear IPAC	Similar to the standard IPAC case, but with the target tropical zonal wind profile $U_T = 0$ at all levels below 150 hPa
HOMRAD IPAC	Similar to the standard IPAC case, but with the calculated radiative temperature tendency zonally homogenized at each time step between 10°S and 10°N
HOMFLX IPAC/EPAC	Similar to the weak-jet IPAC/EPAC cases, but with the calculated surface heat and moisture fluxes zonally homogenized at each time step between 10°S and 10°N
CNTL-D	Variant of the control case, in which damping of extratropical eddies is applied at all latitudes poleward of 30°, while the zonal-mean temperature, moisture, and horizontal winds are nudged everywhere toward their simulated distributions in the control case
IPAC-D/EPAC-D	Similar to CNTL-D, but where nudging of the zonal-mean temperature, moisture, and horizontal winds is toward their simulated climatological distributions in the standard IPAC/EPAC case
Weak-jet IPAC-D	Similar to IPAC-D, but where nudging of the zonal-mean temperature, moisture, and horizontal winds is toward their simulated climatological distributions in the weak-jet IPAC case

time-mean subtropical jet between 20° and 30° (left and right panels, respectively). Both spectra show clear evidence of eastward-moving "storm-track" disturbances (e.g., Pratt, 1977), whose dispersion and peak zonal wavenumbers at $k = 4$ and 5 are strikingly reminiscent of the non-classical Kelvin wave signals seen previously in Figure 2d. As shown by the gray curves in each panel, the dispersive nature of these extratropical signals is well captured by that theoretically expected for non-divergent Rossby waves on the sphere under the effects of Doppler-shifting by a mean zonal flow, that is,
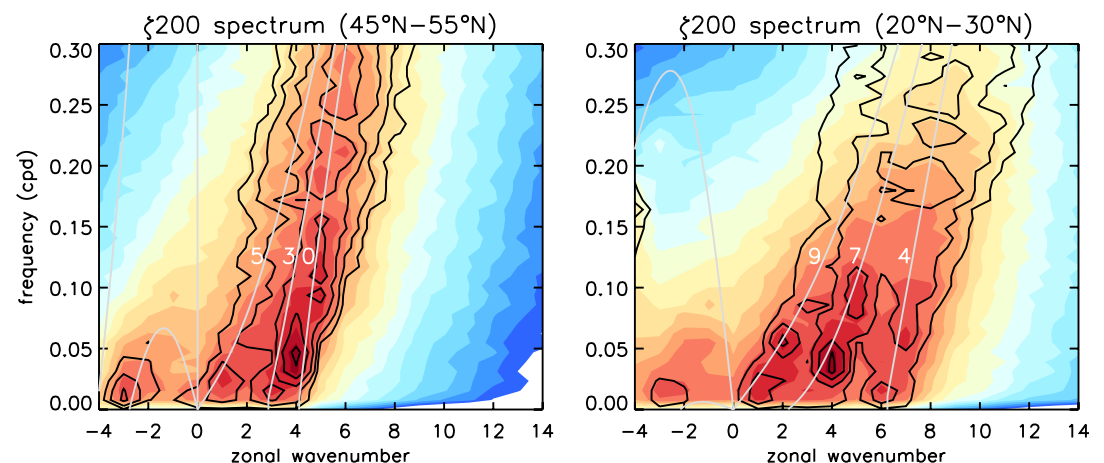

Figure 4. Average space-time spectrum of vorticity at 200 hPa (ζ200) for the latitude bands: (a) 45°–55° and (b) 20°–30°, Gray curves with labels in each panel denote the theoretically predicted dispersion of Doppler-shifted Rossby waves on the sphere in Mercator coordinates for different meridional wavenumbers l (see text for details).

$$\omega = kU_m - \frac{k\beta_m}{k^2 + l^2}, \tag{6}$$

where the subscript m denotes a Mercator projection of the sphere (cf. Hoskins & Karoly, 1981), $U_m \equiv U/\cos\phi$ is the background zonal wind (with ϕ as latitude), β_m is the meridional gradient of the absolute vorticity (scaled by $\cos\phi$), and k and l are the (Cartesian) zonal and meridional wavenumbers, respectively. The various curves in Figures 4a and 4b are for different integer values of l, with U_m and β_m taken as their simulated climatological averages at 300 hPa for the center of the latitude band of interest. The overall correspondence points to eddies in the subtropics has having significantly larger values of l, as compared to eddies at higher latitudes, with l being larger in both cases for smaller values of k. As discussed in Appendix B, reasonable agreement is found when comparing these implied regional variations in l versus k against actual regional horizontal (k–l) wavenumber spectra of $\zeta 200$. The reason for the dominance of signals at $k = 4$ and 5 in both cases is presumably tied to the preferred scales of baroclinic instability in the midlatitudes (Pratt, 1977; Randel & Held, 1991).

3.2. Composite View of Extratropical Forcing

The similarities between the subtropical vorticity spectrum in Figure 4b and the tropical rain spectrum in Figure 2d suggests that lateral forcing of the tropics by midlatitude eddies may be essential for eliciting the non-classical dispersion, as well as preferred zonal scales, of the simulated Kelvin wave disturbances. Evidence to support this idea can be found in Figure 5a, which depicts the composite 200-hPa horizontal flow and vorticity anomaly patterns associated with individual wave disturbances in filtered tropical rain, where details about the compositing technique are described in the figure caption. The patterns appear very similar to those documented by Straub and Kiladis (2003a, hereafter SK03) in the context of extratropical-forced Kelvin waves over the central tropical Pacific (see their Figure 2 and also Roundy, 2014). A noteworthy feature is the positively tilted Rossby wave train in the extratropics, implying equatorward propagation of wave energy to the west (i.e., "upstream") of the simulated Kelvin wave's convective envelope. The anticyclone on the immediate poleward flank of this envelope, together with straddling cyclones to the east and west, is also reminiscent of SK03's observations. While such off-equatorial gyres are not present in β-plane Kelvin waves (which have no meridional wind), Figure 5b shows that the composite structure in the lower troposphere (850 hPa) is indeed Kelvin-like, with winds that are predominantly oriented in the zonal direction and roughly in-phase with the geopotential height field, very similar to that observed by SK03 (see their Figure 5). The extratropical wave train is centered in this case at around 40°N and shows little evidence of equatorward propagation, suggesting that the pathway of extratropical forcing lies in the upper troposphere near the level of the subtropical jet core.

3.3. On the Mechanism of the Extratropical Forcing

What is the precise mechanism responsible for this apparent extratropical forcing? The working hypothesis here is that the answer involves the effects of transient Rossby wave dissipation due to critical layer absorption in the subtropical upper troposphere. Generally speaking, such absorption occurs when an equatorward-propagating Rossby wave encounters a critical latitude (or line) where the zonal velocity of the wave's crests and troughs matches that of the local background zonal flow, that is, $U - c = 0$ (Bennet & Young, 1971). A well-known effect of this process is the deposition of the eddy momentum flux, which acts as transient source of zonal momentum, both in a zonal-mean *and* local perturbation sense (Randel & Held, 1991). The interest here is in the latter sense, specifically in terms of the forcing of individual wavenumbers and frequencies, that is,

$$\langle F \rangle \equiv -\langle \nabla_H \cdot \boldsymbol{m} \rangle, \tag{7}$$

where $\langle \cdot \rangle$ denotes the space-time Fourier transform operator and $\nabla_H \cdot \boldsymbol{m}$ is the divergence of the horizontal eddy flux of zonal momentum in pressure coordinates. The latter is given by: $\langle \boldsymbol{m} \rangle = (\langle u \rangle \langle u \rangle^*, \langle u \rangle \langle v \rangle^*)$, where $\langle \cdot \rangle^*$ denotes the complex conjugate. The fact that F occurring outside of the tropics can act to excite (dry) equatorial Kelvin modes is well supported by theoretical work of Hoskins and Yang (2000). As those authors point out, the only requirement is that F projects onto the Kelvin mode's zonal wind eigenstructure.
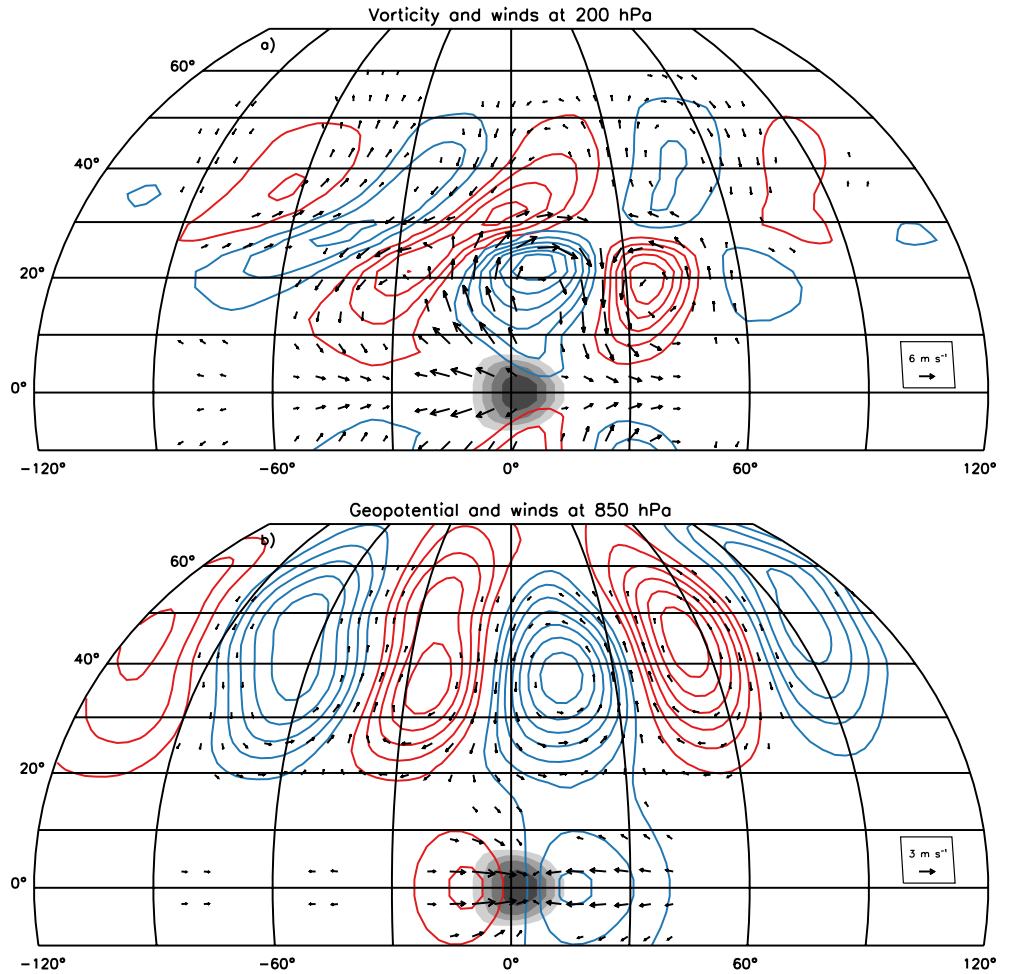
Figure 5. Simultaneous composite maps at (a) 200 and (b) 850 hPa of the equatorially symmetric component of various bandpass-filtered (2–120-day) atmospheric quantities associated with moist Kelvin wave disturbances in the control simulation. Vectors in panel (a) denote horizontal wind anomalies with speed >2 m s^{-1} and statistical field significance $>95\%$; vectors in panel (b) are similar, but for speed >1 m s^{-1}. Red (blue) contours in panel (a) denote positive (negative) relative vorticity anomalies, with intervals of 3×10^{-5} s^{-1} and the zero contour omitted. Contours in panel (b) are similar, but for geopotential height anomalies with intervals of 3 m. Shading in both panels denotes positive surface rain anomalies, with intervals of 0.2 mm hr^{-1} and the zero contour omitted. Kevin wave disturbances are identified using a filtered object-based approach, similar to that described in Tulich and Kiladis (2012). Briefly, objects are defined as contiguous regions in the longitude-time domain where filtered rain anomalies averaged between 5°S and 5°N exceed a threshold; the object filter retains eastward-moving wavenumbers in the range 1–14, with periods in the range 2–120 days. Composite averaging is performed relative to the set of base points in the longitude-time domain where object-filtered rain anomalies exceed one standard deviation of their respective object's distribution.

To evaluate this forcing pathway in the model, the Kelvin-mode projection of F is calculated as:

$$F_{\mathrm{K}} = \frac{1}{\pi} \int_{-\pi/2}^{\pi/2} w_r(\phi) F(x, \phi, p, t) \exp[-(\phi/2\phi_*)^2] d\phi, \tag{8}$$

where ϕ_* is the meridional trapping-scale parameter of Gill (1980) and w_r is a weighting function intended to isolate the contribution to F_{K} by "remote" eddies, as opposed to those internal to the tropics, that is,

$$w_r = \begin{cases} 1 & \text{if } |\phi| \geq 15°, \text{ and} \\ 0 & \text{otherwise.} \end{cases} \tag{9}$$

Conversely, the Kelvin-mode projection of u is calculated as:

$$u_{\mathrm{K}} = \frac{1}{\pi} \int_{-\pi/2}^{\pi/2} w_t(\phi) u(x, \phi, p, t) \exp[-(\phi/2\phi_*)^2] d\phi, \tag{10}$$
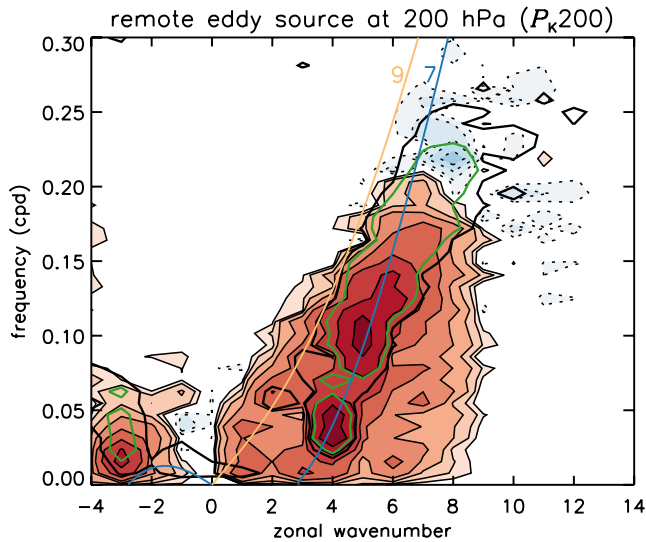
Figure 6. Average space-time spectrum of the Kelvin-projected remote eddy source (Equation 11,12) at 200 hPa ($P_K 200$) in the control simulation, where red (blue) shading denotes positive (negative) values, with logarithmic intervals between 2×10^{-5} and $5 \times 10^{-3}\,\mathrm{m^2\,s^{-2}\,day^{-1}}$. Heavy black and green contours denote where the signal-to-noise ratio of the simulated tropical rain spectrum is significantly greater than one at the 90% and 99% confidence levels, respectively. Rossby-wave dispersion curves are similar to those in Figure 4b.

where w_t is essentially the inverse of w_m, that is,

$$w_t = \begin{cases} 1 & \text{if } |\phi| \le 15°, \text{ and} \\ 0 & \text{otherwise.} \end{cases} \tag{11}$$

The form of the latter weighting function, together with Equation 10, is very similar to that adopted in previous equatorial wave studies by Yang et al. (2003) and Gehne and Kleeman (2012). Somewhat different from these studies, however, the value of ϕ_* is taken here as 9°, as opposed to 6°, corresponding to a dry Kelvin/gravity wave speed $c_* = 45\,\mathrm{m\,s^{-1}}$, as opposed to $20\,\mathrm{m\,s^{-1}}$. The rationale stems from an analysis in Appendix C, which shows that moist Kelvin wave variability in the model, as well as in observations, is characterized by leading meridional structures in upper-level zonal wind that are well captured by that theoretically expected for dry Kelvin waves with $\phi_* = 9°$ or even larger. The fact these zonal wind structures have non-negligible amplitude in the subtropics, as shown in Figure C1, is a necessary condition for enabling their potential forcing by midlatitude eddies, as embodied mathematically in Equations 8 and 9.

Such remote forcing by itself, however, does not guarantee that Kelvin mode circulations in the tropics will be energetically maintained, since the latter requires a positive correlation between fluctuations in u_K and F_K. The following quantity is therefore of primary interest in this study:

$$P_K(k,\omega) = 2\mathrm{Re}\left(\langle u_K \rangle \langle F_K \rangle^*\right), \tag{12}$$

where P_K is termed the "remote eddy source" and represents the production of Kelvin-mode kinetic energy KE_K in Fourier space due to correlated variations between $\langle u_K \rangle$ and $\langle F_K \rangle$. Figure 6 depicts the average spectral distribution of P_K at 200 hPa, denoted $P_K 200$, in the control simulation. The signals of the model's eastward-moving tropical waves, denoted by the heavy black and green contours, are generally well matched by *positive* signals in $P_K 200$ (red shading), suggesting that the simulated waves are indeed mechanically forced by Rossby-type eddies in the subtropical upper troposphere, with preferred meridional wavenumbers in the range $l = 7$–9. However, because tropical convection can generally act as a source of Rossby wave energy in the subtropics, especially in the presence of a strong subtropical jet (cf. Sardeshmukh & Hoskins, 1988), the possibility of the reverse forcing pathway cannot be ruled out. More discriminating tests aimed at addressing this issue are described in Section 5.

3.4. Remote Eddy Forcing Versus Local Tropical Heating

How does this remote eddy forcing compare to that due to "local" heating internal to the tropics? To address this question, the production of Kelvin-mode *available potential* energy PE_K is first calculated as:

$$H_K = 2\mathrm{Re}\left(\langle T_K \rangle \langle Q_K \rangle^*\right) R_d / \sigma_0, \tag{13}$$

where R_d is the dry air gas constant, σ_0 is the model's climatological (pressure-weighted) static stability profile in the tropics, T_K is the local Kelvin-mode component of the simulated temperature, and Q_K is the local Kelvin-mode component of the superparameterized temperature tendency. The latter two quantities are both calculated using the same (tropical) weighting function w_t as for the zonal wind quantity u_k. The individual sums of H_K and P_K are then taken over the set of eastward-moving spectral bins where the signal-to-noise ratio of the model's tropical rain spectrum is significantly greater than one at the 99% confidence (denoted by the green contour in Figure 6). The resulting aggregate quantities are denoted as $\boldsymbol{H}_K$ and $\boldsymbol{P}_K$, where the former represents the net source of PE_K due to the effects of *local* tropical heating, while the latter represents the net source of KE_K due to the effects of *remote* eddy forcing in the extratropics (i.e., poleward of 15°).

Figure 7a depicts the vertical profiles of $\boldsymbol{H}_K$ and $\boldsymbol{P}_K$, as diagnosed in the control simulation. The tropical heating source $\boldsymbol{H}_K$ is quasi-sinusoidal in appearance, with positive values in the upper troposphere between
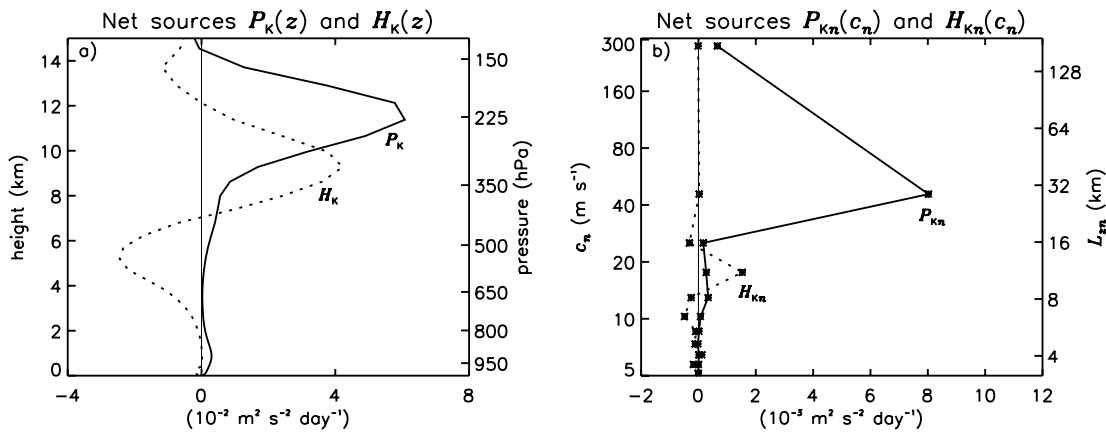
Figure 7. (a) Vertical structures of the net remote eddy and tropical heating sources, P_K (solid) and H_K (dotted), respectively, in the control simulation. (b) similar to panel (a), but where the respective energy sources are plotted in terms of their vertical-mode forms P_{Kn} and H_{Kn}.

roughly 7 and 12 km and negative values above and below. The remote eddy source P_K, on the other hand, is positive at all levels (which is not guaranteed) with signals confined mainly between 8 and 14 km. The fact that both energy sources are peaked in the upper troposphere is consistent with what has been inferred for Kelvin waves in the real world, based on their tilted boomerang-like structures in the vertical in both temperature and zonal wind (SK03; Kiladis et al., 2009; Straub & Kiladis, 2003b). As shown in Figure 8, similar tilted structures are readily apparent in composites of the simulated waves, with the "elbows" of the boomerangs occurring at roughly the same altitude as where their respective energy source is strongest (indicated by the dashed green lines). Results in Figure 8a also help to explain why the net energy production due to tropical heating H_K tends to be substantially negative in the middle to lower troposphere, owing to deep convective heating being preferentially enhanced when the lower half of the atmosphere is anomalously cold. Conversely, as evidenced by the phasing between F_K and u_K in Figure 8b, the reason for the strong eddy-driven production of energy in the layer between 10 and 12 km is due mainly to the eddy forcing being strongly negative to the immediate west of the convective envelope, where the zonal wind is also strongly negative, as part of the envelope's upper-level divergent outflow. Vertical integration of the profiles in Figure 7a yields a picture in which the waves are primarily driven by mechanical forcing in the extratropics, as opposed to local tropical heating.
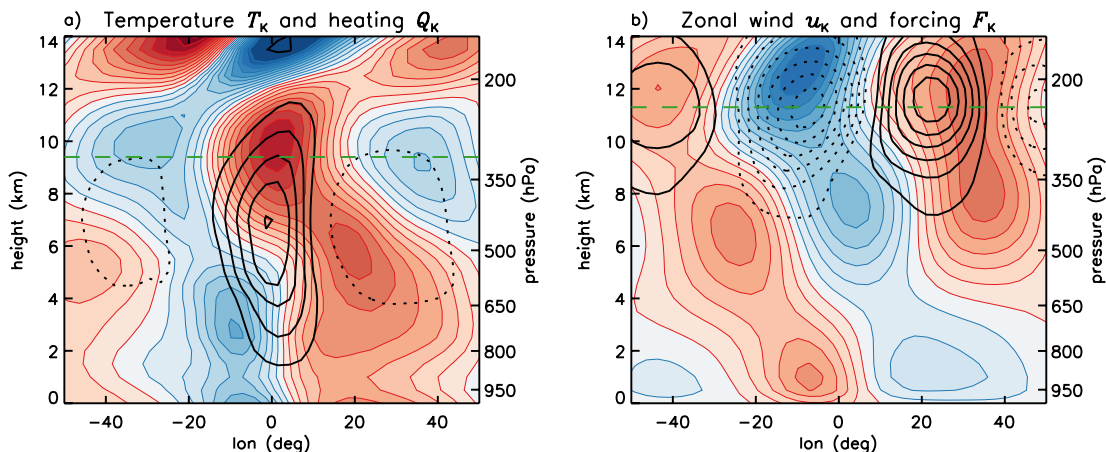

Figure 8. Composite longitude-height structures of the simulated Kelvin waves in the control simulation in terms of either: (a) Kelvin-mode temperature T_K (shading) and superparameterized heating Q_K (contours) or (b) Kelvin-mode zonal wind u_K (shading) and resolved eddy-momentum forcing F_K (contours). Red/blue shading denotes positive/negative values with intervals of 10^{-2} K for T_K and 10^{-2} m s^{-1} for u_K. Solid/dotted contours are similar but with intervals of 2×10^{-1} K day^{-1} for Q_K and 2×10^{-1} m s^{-1} day^{-1} for F_K. Dashed green lines denotes the level where the net Kelvin-mode energy source of the associated variable (i.e., H_K for T_K; P_K for u_K) is at its largest.

Table 2
Calculated Phase Speeds c_n and Bulk Vertical Wavelengths L_{zn} for the First 10 Vertical Modes in the Control Simulation

n	0	1	2	3	4	5	6	7	8	9
c_n (m s^{-1})	278	45.7	25.2	17.6	12.9	10.3	8.59	7.36	6.44	5.73
L_{zn} (km)	175	28.6	15.8	11.1	8.13	6.46	5.39	4.62	4.05	3.60

3.5. Vertical Mode Energetics

Another useful way of viewing the energetics of moist tropical waves is in terms of a discrete set of vertical normal modes, where the latter conveys information about the spectrum of vertical wavelengths that are energetically maintained by the forcing. Such information is key for addressing fundamental questions about how the forcing acts to modulate the convection field and vice versa. Here, the vertical orthonormal modes (and their associated "phase speeds" c_n) are calculated as in Tulich et al. (2007), but with a rigid lid assumed at 150 hPa, as opposed to the model top. The modal forms of $\boldsymbol{H}_K$ and $\boldsymbol{P}_K$ are then calculated respectively as:

$$H_{Kn} = \sum 2\mathrm{Re}\left(\langle T_{Kn}\rangle\langle Q_{Kn}\rangle^*\right), \text{ and } P_{Kn} = \sum 2\mathrm{Re}\left(\langle u_{Kn}\rangle\langle F_{Kn}\rangle^*\right), \tag{14}$$

where $(\cdot)_n$ denotes the nth mode's contribution to the corresponding dynamical field, and the summation is over the same set of wavenumber-frequency bins as described previously. Note that these modal forms are related to their physical-space forms via the Parseval rule, which states that the sum of the former over n is mathematically equivalent to the mass-weighted vertical average of the latter (Fulton & Schubert, 1985).

Conceptually, the vertical modes are very much like Fourier modes, but with oscillatory structures that deviate somewhat from pure sinusoids, owing to vertical variations in the background static stability. Nevertheless, Tulich et al. (2007) showed that a "bulk" vertical wavelength L_{zn} can meaningfully be assigned to each mode, based on the analytic expression for Kelvin/gravity waves in a Boussinesq atmosphere with constant static stability, that is,

$$L_{zn} \equiv \frac{2\pi c_n}{N_0}, \tag{15}$$

where $N_0 = 1 \times 10^{-2}$ s^{-1} is a representative value of the Brunt-Väisällä frequency in the troposphere. As a relevant example, the $n = 1$ mode has an associated phase speed $c_n \approx 46$ m s^{-1} and thus, a bulk vertical wavelength $L_{zn} \approx 29$ km, or roughly two times the depth of the troposphere. The remaining higher-order modes have values of c_n and L_{zn} that vary approximately as $1/n$, as illustrated in Table 2.

As might be expected on the basis of their contrasting vertical structures, Figure 7b shows that the relative contributions of the net tropical heating and remote eddy sources, denoted by the black dotted and solid curves, respectively, are quite different in terms of their vertical mode projections: the remote eddy source P_{Kn} acts mainly as a strong driver of the $n = 1$ mode, as seen by its pronounced spectral peak at $c_n \approx 46$ m s^{-1} ($L_{zn} \approx 29$ km); the tropical heating source H_{Kn}, on the other hand, acts mainly as a much weaker driver of the $n = 3$ mode with $c_n \approx 18$ m s^{-1} ($L_{zn} \approx 11$ km). Because the $n = 1$ mode is generally known to be more effective in promoting tropical deep convection, via destabilization of the entire column, as compared to the shallower $n = 3$ mode (given equal amplitude temperature perturbations; Tulich & Mapes, 2010), these results support the interpretation that extratropical forcing of the $n = 1$ mode is indeed the primary driver of the simulated Kelvin waves. However, the picture is not as straightforward as it seems, since a portion of this remote eddy forcing is actually driven in turn by the effects of tropical heating, as shown later in Section 5.

4. Model Sensitivity to Changes in the Background Zonal Flow

Having established an important link between the extratropics and the model's eastward-moving tropical wave spectrum in the control setup, this section describes how the picture changes in response to imposed changes in the structure of the background zonal flow. The description begins with a focus on the standard IPAC and EPAC integrations, where nudging of the zonal-mean zonal wind [u] is applied only in the tropics.
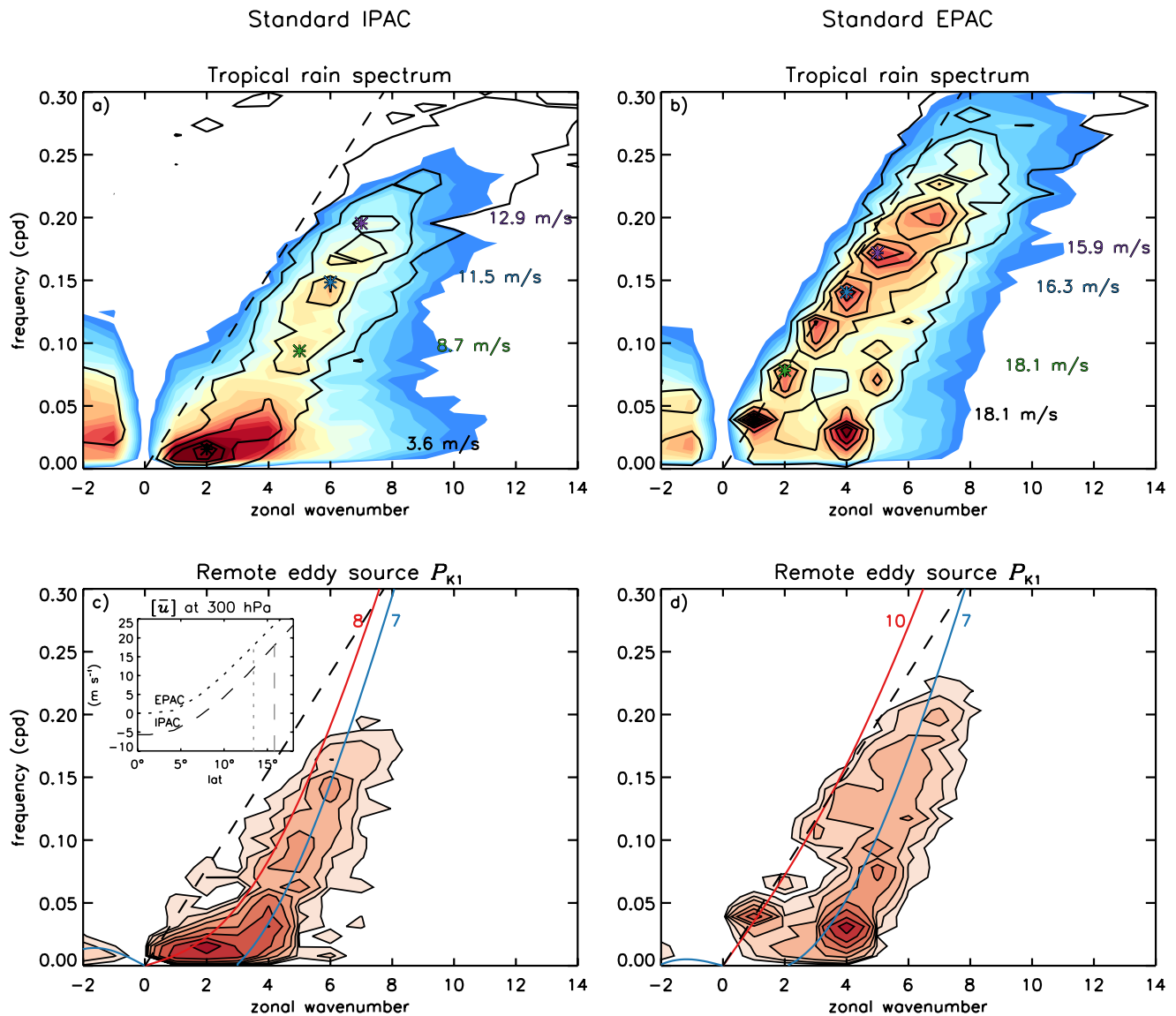
Figure 9. Tropical rain spectra in the standard (a) IPAC and (b) EPAC integrations, following the same plotting convention as in Figure 2d. Bottom panels are similar, but for the $n = 1$ remote eddy source P_{K1}, where red/blue shading denotes positive/negative values with levels ranging logarithmically between 2×10^{-5} and $2 \times 10^{-3} \, \mathrm{m^2 \, s^{-2} \, day^{-1}}$. Sloping dashed line in each panel denotes a constant phase speed of $18 \, \mathrm{m \, s^{-1}}$. Inset in panel (c) compares the simulated background zonal wind profiles at 300 hPa in IPAC (dashed) versus EPAC (dotted), where the vertical gray lines denote the critical latitudes of Rossby waves with $c = 18 \, \mathrm{m \, s^{-1}}$. Rossby wave dispersion curves in panels (c) and (d) were calculated as in Figure 4b, but with values of l chosen to correspond to underlying features in P_{K1}.

4.1. Standard IPAC and EPAC Cases

Figures 9a and 9b display the mean eastward-moving tropical rain spectra obtained in the standard IPAC and EPAC cases, respectively. Broad agreement is seen when comparing these spectra against their observed regional counterparts in Figure 1. The spectrum in the IPAC case shows a pronounced MJO-like spectral peak at $k = 2$, in addition to a lobe of relatively slow-moving and dispersive Kelvin waves, much like in the observed regional spectrum of Figure 1a. Conversely, the spectrum in the EPAC case is dominated by faster-moving and more classical Kelvin wave signals, much like in the observed regional spectrum of Figure 1b. This favorable agreement is remarkable and indicates that much of the observed regionality of Kelvin waves and the MJO can be attributed mainly to regional variations in the background zonal flow, as opposed to regional variations in mean-state moisture and/or temperature. Favorable agreement is also
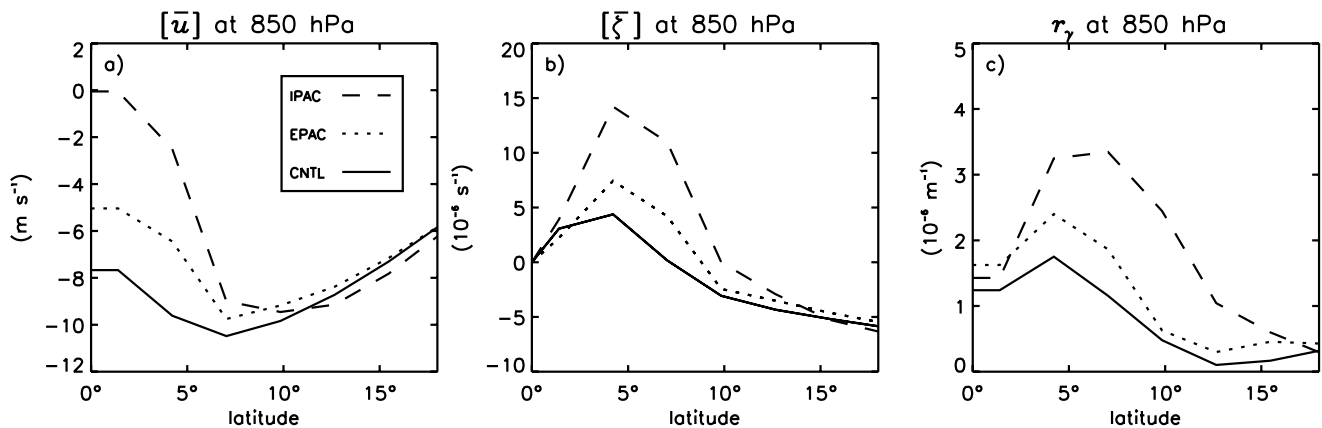
Figure 10. Meridional profiles at 850 hPa of the (a) background zonal wind $[\bar{u}]$, (b) background relative vorticity $[\bar{\zeta}]$, and (c) the coefficient of linear regression r_γ between intraseasonal (35–120-day) fluctuations in u_K and the absolute value of high-frequency (< 25-day) fluctuations in the antisymmetric component of the relatively vorticity ζ_A, as diagnosed in CNTL (solid), IPAC (dashed), and EPAC (dotted).

found when comparing the composite dynamical structure of the simulated MJO-like mode of variability in the IPAC case against that documented for the MJO on Earth by previous authors (see Appendix D).

To help interpret these results, Figures 9c and 9d compare the space-time spectra of the $n = 1$ remote eddy source P_{K1} for the two cases. The strong mirroring of the signals in precipitation and P_{K1} (e.g., at $k = 1$ in Figures 9b and 9d) is telling and points to changes in the spectrum of eddy phase speeds (and meridional wavenumbers) capable of forcing Kelvin wave motions at the equator. These changes can be understood, at least in a qualitative sense, by considering the inset in Figure 9c, which shows how the background zonal flow (denoted $[\bar{u}]$) is altered in response to the nudging, not only in the deep tropics, but also in the subtropics at upper levels, due to angular momentum being approximately conserved in the poleward flowing branch of the model's Hadley circulation. The net effect, as indicated, is that Rossby waves with a representative phase speed of 18 m s^{-1} have their critical latitude shifted from roughly 16° to 13° in the IPAC versus EPAC basic states, a shift that apparently enables these relatively fast-moving waves (with larger preferred values of l) to more strongly drive similarly fast-moving Kelvin-mode circulations at the equator in EPAC, via their enhanced projection. Unlike in the CNTL case, however, an important role of the $n = 1$ tropical heating source H_{K1} is also found for these planetary-scale Kelvin wave signals, in addition to the slower-moving MJO-like signals in the IPAC case (results not shown), suggesting that mechanisms involving convection-wave interactions internal to the tropics may be a further causal factor. Preliminary evidence to support this idea is outlined in the paragraphs below, with additional evidence presented later in Section 5.

4.2. The Critical Role of Mean-State Cyclonic Shear at Low Levels

As just mentioned, the net effect of the nudging on the background zonal flow $[\bar{u}]$ extends well into the subtropics in the upper part of the troposphere. The story is quite different in the lower troposphere, however, where the changes in $[\bar{u}]$ tend to be confined to the deep tropics, owing to the mean meridional winds being directed equatorward. This confinement is readily apparent in Figure 10a, which compares the meridional structure of $[\bar{u}]$ at 850 hPa among the three different cases (i.e., CNTL, EPAC, and IPAC). Because strong easterlies prevail outside of the nudging zone, the net effect of the nudging, as shown in Figure 10b, is to enhance the ambient level of cyclonic shear (i.e., $[\bar{\zeta}] > 0$ for the northern hemisphere) between roughly 3° and 10° latitude. The enhancement is especially noteworthy in the IPAC case, where peak values of $[\bar{\zeta}]$ are roughly double those in the EPAC case, while being more than triple those in the CNTL case. To address whether it is this enhancement in meridional shear, as opposed to the introduction of easterly shear in the vertical, that is, responsible for the development of MJO-like variability in the IPAC case, an additional simulation was performed (referred to as "no-shear IPAC"), in which the easterly shear was removed by setting $U_T = 0$ at all levels below 150 hPa. The resulting spectrum was found to still contain signals resembling the MJO, but with total variance reduced by roughy 20%, apparently due to a corresponding reduction in the

remote eddy source P_{K1} (see Figure S2). Given this result, it is concluded that the primary reason for the emergence of MJO-like variability in the IPAC case is indeed tied to the introduction of anomalous low-level mean westerlies at the equator and the resultant increase in $[\bar{\zeta}]$.

As alluded to in the introduction, one possible explanation for this result is that the SIEM mechanism of MJO propagation (involving the disturbance's modulation of high-frequency eddy activity and the associated lateral mixing of moisture) is amplified in the IPAC case, owing to the effects of non-linearities being magnified by the larger mean cyclonic shear (Wang et al., 2019). To explore this idea, the following linear regression model was constructed using the model output at 850 hPa:

$$\left|\zeta_A^H\right| = r_\gamma u_K^B, \tag{16}$$

where the superscript "H" denotes application of a 25-day highpass filter, the superscript "B" denotes application of a 35–120-day bandpass filter, ζ_A is the antisymmetric component of the vorticity, and r_γ is the regression coefficient (which is calculated at each latitude and longitude). The intent is to draw a direct analogy with the linear parameterization of the SIEM mechanism in Equation 1, as first proposed by Sobel and Maloney (2013).

Figure 10c compares the meridional distribution of (r_γ) among the three different cases. The fact that the distributions are everywhere positive in all cases, with peak values located at or near the center of the peak shear zone, is supportive of the choice of $\gamma > 0$ and the physical concepts underlying this choice. However, rather than being constant, it appears based on Figure 10c that the strength of the SIEM mechanism is indeed strongly dependent on the degree of mean-state cyclonic shear, such that MJO-like modes of variability are evidently rendered unstable in the IPAC basic state, compared to being either near neutral or damped in the remaining two basic states. Additional work is needed to clarify the mechanisms underlying this mean-flow dependence of the SIEM mechanism, which is beyond the scope of this study.

Interactions between convection and radiation are also found to be essential for the simulated MJO-like variability. Repeating the standard IPAC integration, but with the effects of these interactions suppressed (corresponding to the HOMRAD IPAC case in Table 1) yields a tropical rain spectrum that is largely devoid of any sort of coherent intraseasonal modes of variability, being instead dominated by the signals of traditional higher-frequency Kelvin waves with phase speeds in the range 11–15 m s^{-1} (see Figure S3). This sort of tropical wave response is similar to that seen in previous MJO modeling work by Andersen and Kuang (2012) and Ma and Kuang (2016). Meanwhile, in looking at the column-integrated moist static energy (MSE) budget of the model's MJO analog for the tropical belt 10°S–10°N (calculated as in Andersen & Kuang, 2012; see Figures 11a and 11b), the picture is found to broadly resemble that documented for the MJO on Earth by Ren et al. (2021), where longwave radiation feedbacks (denoted "LW") act as the primary amplifier of the disturbance (but tend to oppose its eastward propagation), while the horizontal advection of MSE (denoted "hAdv") acts as the primary driver of propagation (but tends to oppose amplification). This dichotomy can be understood on the basis of Figure 11c, which shows that zonal fluctuations in hAdv tend to be shifted roughly 90° to the east of those in both LW and column-integrated MSE, apparently due to the effects of the SIEM mechanism. The overall impression is that of a symbiotic interaction between LW and hAdv, in which both are equally essential for MJO existence and propagation (in accordance with the theory of Sobel & Maloney, 2013), but where the relative importance of hAdv is also crucially dependent on the strength of the mean cyclonic shear at low levels (as implied by Figure 10c).

4.3. Weak-Jet Cases

The above findings indicate that the meridional structures of the background zonal flow in both the upper and lower troposphere are important for shaping the model's eastward-moving tropical wave spectrum. To further explore the role of the upper-level mean flow structure, Figure 12 documents the changes that arise in response to an imposed 25% weakening of the subtropical jet. The overall reduction in eastward-moving tropical wave variability and remote eddy production (P_{K1}) is qualitatively consistent in both cases with expectations based on critical-line arguments, where the slower mean westerlies should act to inhibit the lateral forcing of the tropics by equatorward-propagating eddies in the midlatitudes, especially at faster phase speeds. In addition to this overall weakening, however, both tropical rain spectra show significant changes
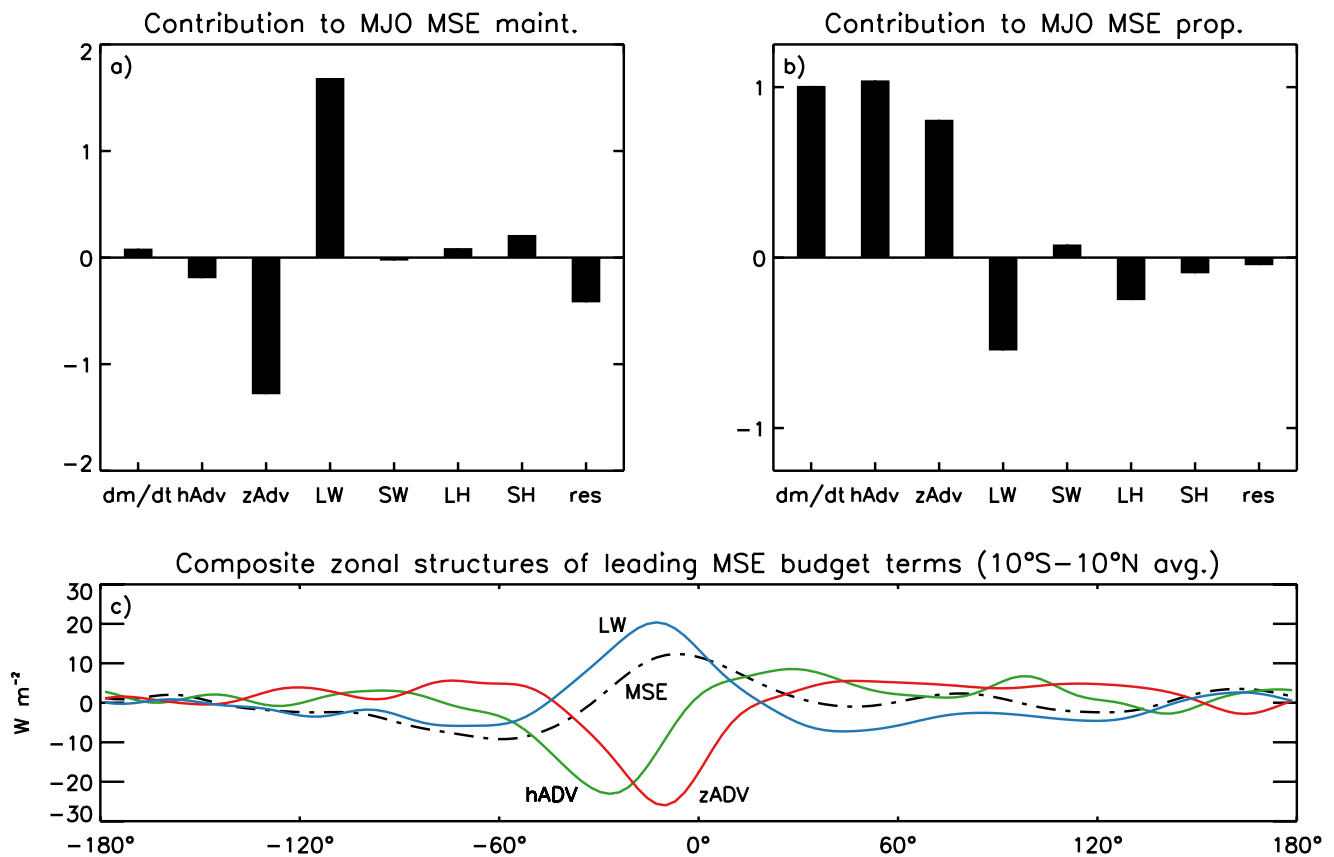
Figure 11. Select results from a column-integrated MSE budget analysis of the composite MJO analog produced in the standard IPAC case, calculated as in Andersen and Kuang (2012) for the tropical belt 10°S–10°N. Top panels: normalized contributions to the (a) maintenance (with units: $10^{-1}\,\mathrm{day}^{-1}$) and (b) propagation of column-integrated MSE anomalies. Labeled contributions are for the column-integrated MSE tendency (dm/dt), horizontal advection tendency (hAdv), vertical advection tendency (zAdv), longwave radiation tendency (LW), shortwave radiation tendency (SW), surface latent heat flux (LH), surface sensible heat flux (SH), and the budget residual (res). Bottom panel (c): Composite zonal distributions of LW (blue), hAdv (green), and zAdv(red), along with the column-integrated MSE (scaled by a factor $10^{-1}\,\mathrm{day}^{-1}$; dot-dashed).

in the character of the simulated intraseasonal variability. The changes in the IPAC case are perhaps the easiest to interpret, where the preferential reduction of MJO-like variability at $k = 2$ and higher appears to stem from corresponding reductions in the remote eddy source P_{K1}.

The story in the EPAC case, however, is more complicated: Figure 12d shows that intraseasonal rain signals are actually enhanced at $k = 1$, despite being reduced virtually everywhere else. Interestingly, broadly similar changes are seen in the signals of P_{K1}, except for a weak enhancement at $k = 2$, where the latter apparently stems from a reduction in the Doppler-shifted phase speed of the faster-moving eddies involved in forcing these planetary-scale wavelengths (compare the $l = 10$ Rossby wave dispersion curves in Figure 12f vs. Figure 9d). The resulting tropical rain spectrum in Figure 12b, which can be regarded as a mixture of relatively fast-moving Kelvin waves and slower-moving MJO-like signals at $k = 1$ and 2, is seen to provide even better agreement with the relevant observed spectrum in Figure 1b, in addition to that documented for the Atlantic sector in Figure 1c. The interpretation is that some amount of shielding of the tropics from the effects of faster-moving eddies in the extratropics (i.e., eddies with $c > 15\,\mathrm{m\,s}^{-1}$) is also necessary for the simulated MJO-like variability. Presumably, the reason why these intraseasonal signals are more muted in this case, as compared to the weak-jet IPAC case, is tied to the weaker mean cyclonic shear in the lower troposphere, through its effect on the SIEM mechanism, as evidenced in Figures 10b and 10c.

Another potential mechanism for the simulated MJO-like variability is that of "wind-induced surface heat exchange" (WISHE), which depends on the presence of mean surface easterlies in the tropics (Emanuel, 1987; Fuchs & Raymond, 2017; Khairoutdinov & Emanuel, 2018; Sentić et al., 2020; Shi et al., 2018). To
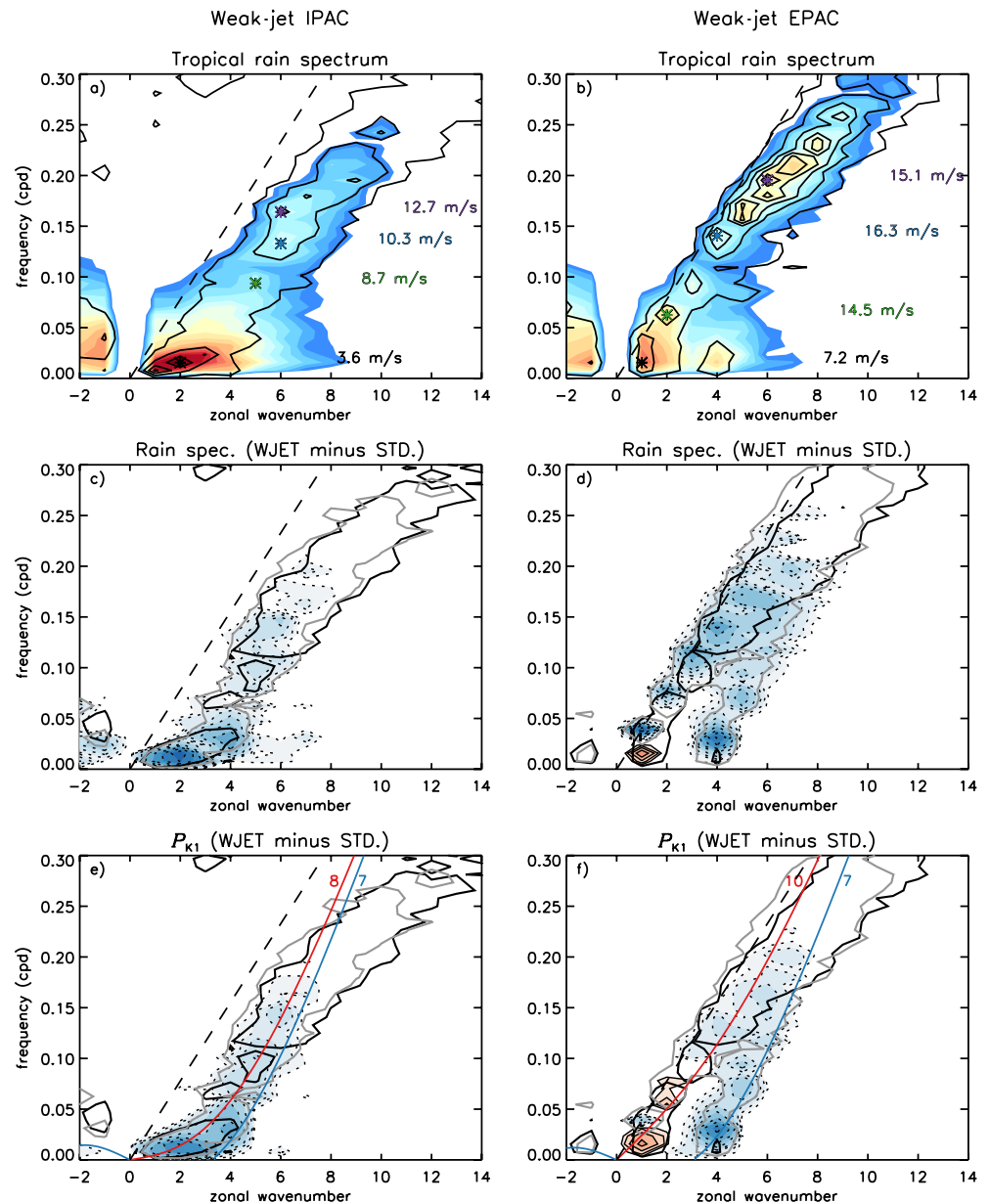
Figure 12. Top panels: similar to Figures 9a and 9b, but for the "weak-jet" (WJET) variants of the IPAC and EPAC cases, respectively. Middle panels: change in tropical rain variance (WJET minus standard), where red/blue shading denotes positive/negative values with logarithmic intervals spanning the same range as in the top panels; heavy black/gray contours denote where the signal-to-noise ratio in the weak-jet/standard spectrum exceeds 1.5 (corresponding to the 90% confidence level). Bottom panels: similar to the middle panels, but for the change in P_{K1}, where shading levels are the same as in Figures 9c and 9d.

assess the importance of this mechanism, the two WJET cases were repeated, but with the surface sensible and latent heat fluxes being zonally homogenized at each time step within 10° of the equator. Results of this experiment (termed HOMFLX, depicted in Figure 13) show that the simulated MJO-like signals are actually enhanced in both cases relative to their original weak-jet counterparts, demonstrating that interactive surface fluxes are not essential to the phenomenon and moreover, tend to have a net damping effect. However, because the signals of low-frequency, westward-moving disturbances in rainfall are also enhanced, the net effect overall is to reduce the percentage of the total intraseasonal (35–120-day) rain variance that is eastward propagating from around 54% to 41% in the IPAC case, and from around 43% to 35% in the EPAC case.
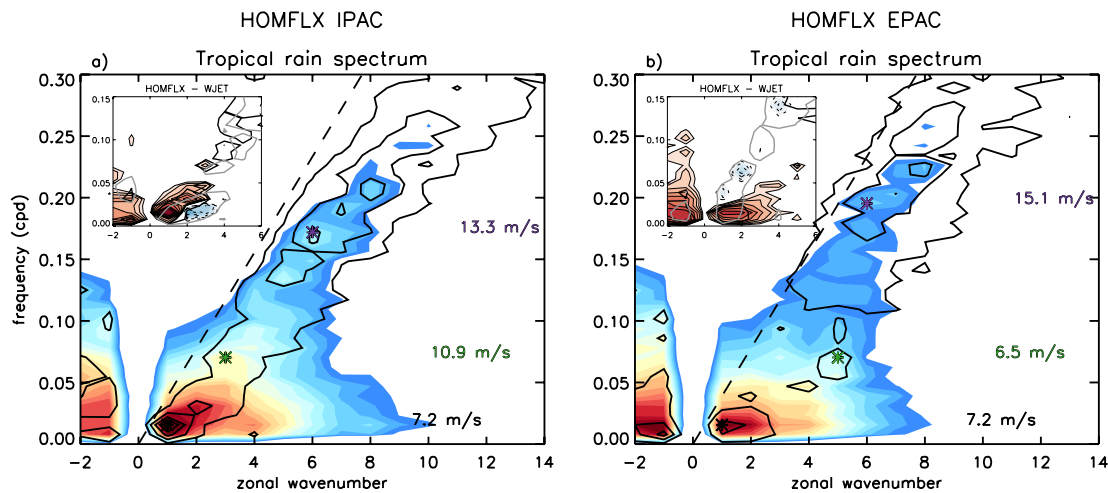
Figure 13. Similar to Figures 12a and 12b, but for the sensitivity experiment, HOMFLX, in which the weak-jet IPAC and EPAC cases were repeated, but with the surface sensible and latent heat fluxes being zonally homogenized at each time step within 10° of the equator. Inset in each panel denotes the change in rain variance relative to the original weak-jet integration for zonal wavenumbers k in the range −2 to +6 and frequencies < 0.15 cpd, following the same plotting convention as in Figures 12c and 12d.

These results differ from those of previous aquaplanet studies, in which the mechanism of WISHE has been found to be essential for the emergence of MJO-like modes variability in free-running climate integrations, distinguished by either globally uniform SSTs (Arnold & Randall, 2015; Khairoutdinov & Emanuel, 2018; Shi & Bretherton, 2014) or SSTs that are spatially uniform within the tropical belt 15°S–15°N (Shi et al., 2018). A drawback to such idealized calculations, however, is that the simulated mean zonal winds are inevitably quite weak, effectively preventing the types of wave-mean-flow interactions demonstrated as being important here.

5. Model Behavior Under Suppression of Midlatitude Eddies

A key issue surrounding the above results concerns the extent to which the simulated differences in eastward-moving tropical wave variability can be attributed to mean-state modulation of convection-wave interactions internal to the tropics versus those involving equatorward-propagating eddies in the subtropics. To address this issue, we present a set of simulations similar to those just reported, but where damping of eddy perturbations about the zonal mean is applied poleward of 30°, to effectively eliminate the forcing of the tropics by midlatitude eddies. This sort of mechanism-denial approach has been become increasingly popular in recent years. Using a global SP model with real-world (as opposed to idealized) lower boundary conditions, for example, Ma and Kuang (2016), hereafter referred to as MK16, showed how damping of midlatitude eddies had little effect on the model's ability to simulate the MJO, provided the underlying basic state was constrained (through a clever combination of nudging and time-invariant forcing) to match that obtained in a free-running reference integration. Here, a similar approach is taken, but where the basic state is maintained strictly through nudging of the zonal-mean temperature, water vapor, and horizontal wind fields. The form of the nudging is the same as in Equation 3, except that nudging timescale τ is increased to 12 h outside of the damping region ($|\phi| \leq 30°$) for all variables, except the meridional wind. The goal once again is to ensure that the simulated time-mean and zonal-mean rain climatology remains close to that obtained in the undamped control case for the tropical domain of interest. Following the approach of MK16, the strength of the eddy damping of all prognostic variables, as measured by the inverse damping time scale, is specified to increase linearly with distance from 0 to 2.7^{-1} day between 30° and 42° and then remain constant thereafter. In the discussion that follows, cases with damping are distinguished from their undamped counterparts using the naming convention, "REF-D," where "REF" identifies the corresponding (undamped) reference integration.
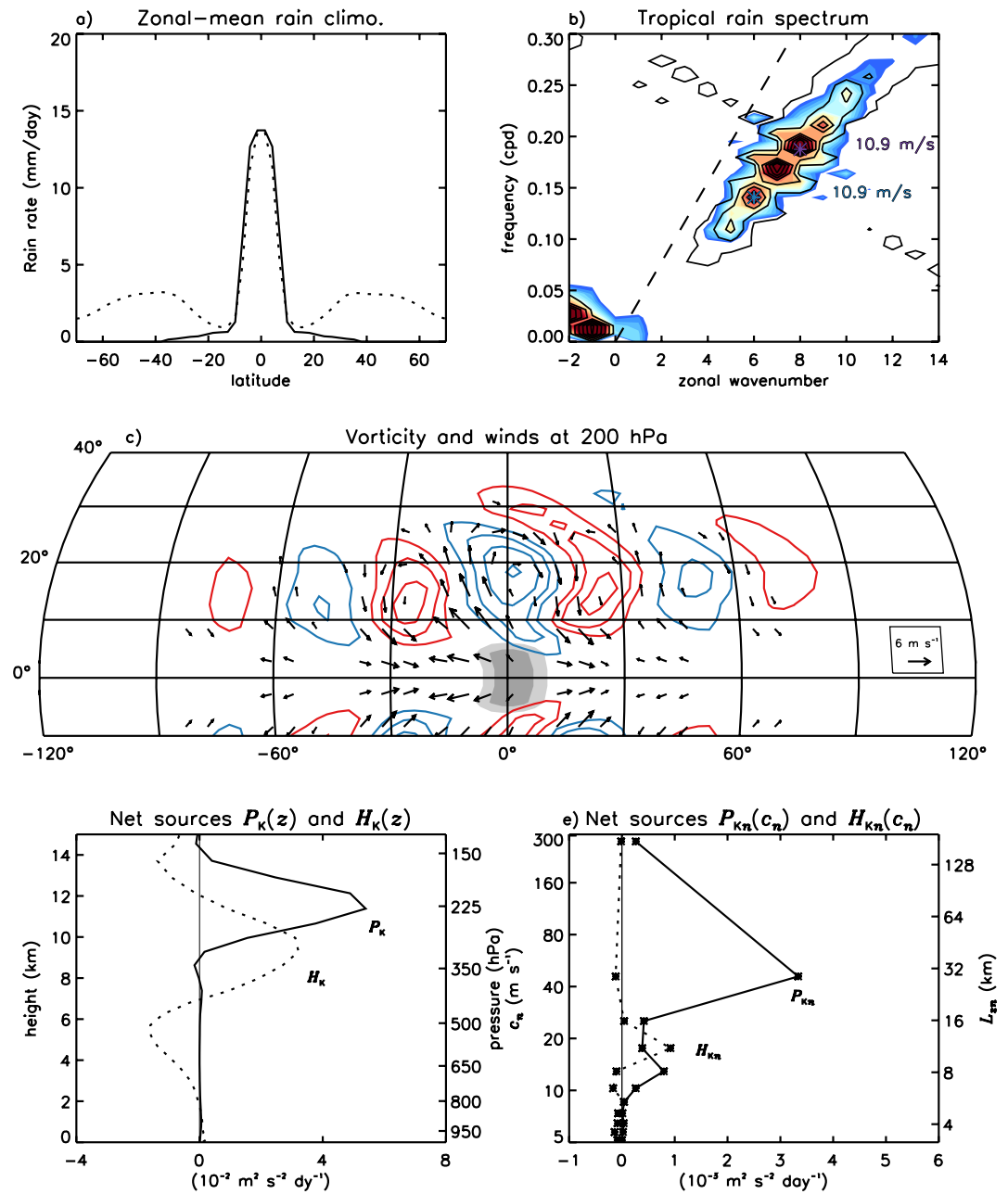
Figure 14. Select results from the eddy-damped version of the control simulation (CNTL-D): (a) Climatological rain distribution in CNTL-D (solid) versus CNTL (dotted); (b) Mean tropical rain spectrum, following the same plotting convention as in Figure 2d, but with a contour interval of 1.2, as opposed to 0.7; (c) Composite maps of 200-hPa vorticity (contours) and horizontal winds (arrows), together with surface rain anomalies (shading), associated with the simulated Kelvin wave disturbances, calculated and plotted as in Figure 5a; (d) Net remote eddy P_K (solid) and tropical heating H_K (dotted) sources; (e) Similar to panel (d), but for the vertical mode forms P_{Kn} and H_{Kn}.

5.1. Effects of Midlatitude Eddy Damping Under the CNTL Basic State

Considering first the eddy-damped variant of the control case (CNTL-D), Figures 14a and 14b show that, while the model's tropical rain climatology remains close to that obtained in the free-running setup (as intended), its spectrum of eastward-moving variability is now markedly different. The waves in this case are almost perfectly non-dispersive, with no indication of the lower-frequency dispersive signals seen

Figure 15. (a–c) Similar to Figures 14b, 14e and 14c, respectively, but for the eddy-damped variant of the standard EPAC integration (EPAC-D).

previously in Figure 2d. The conclusion is that the latter indeed owe their existence to external forcing of the tropics by midlatitude eddies, while the former do not.

Even in this case, however, Figure 14c shows that the composite upper-level structures of the simulated Kelvin waves are still quite unlike those of linear β-plane solutions, with the same sort of flanking subtropical gyre pattern as seen in the reference composite of Figure 5a. Perhaps the simplest explanation for these flanking gyres is that they arise merely as a passive response to convective heating anomalies of the disturbance. Indeed, a Rossby wave source analysis points to the gyres as being mainly forced by the meridional advection of the climatological absolute vorticity by the disturbance's upper-level divergent wind (results not shown). Rather than acting as a passive response, however, it appears on the basis of Figures 14d and 14e that the gyres, once excited, act to return energy back to their parent Kelvin wave, via the same remote forcing pathway as diagnosed in the undamped reference case. Thus, only a portion of the remote eddy source can generally be attributed to the effects of external forcing from the midlatitudes; the remainder is evidently generated by the disturbance itself.

5.2. Effects of Midlatitude Eddy Damping Under the EPAC Basic State

The story is broadly similar when considering the model's response to eddy damping under the EPAC basic state (EPAC-D), defined by mean westerlies aloft. Results in this case, however, show not only the suppression of the slower-moving, dispersive Kelvin wave signals in the synoptic range $k = 4$–6, but also the faster-moving, non-dispersive signals in the planetary-scale range $k = 1$–3 (compare Figure 15a and Figure 9b). Because the phase speed of the missing planetary-scale signals is similar to that of the remaining non-dispersive signals in Figure 15a, the interpretation is that the former are near-neutral "modes," whose emergence requires some level of midlatitude forcing. Meanwhile, comparison of Figures 14e and 15b show that the net contribution of the $n = 1$ remote eddy source P_{K1} is roughly a factor of three smaller than in CNTL-D, while the $n = 3$ tropical heating contribution H_{K3} is more or less the same. Insight into the reduced
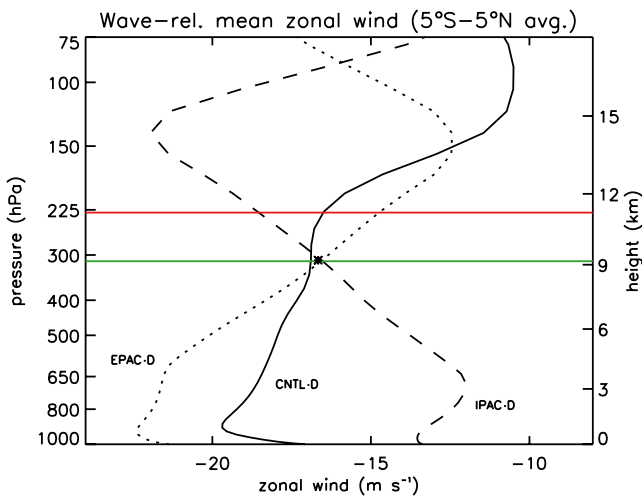
Figure 16. Profiles of the climatological zonal wind (averaged between 5°S and 5°N) in CNTL-D (solid), EPAC-D (dotted), and IPAC-D (dashed), where different constant offsets have been added to allow comparison in the wave's moving frame of reference; the offsets were selected on the basis of the corresponding simulation's tropical rain spectrum as: 10.9 (CNTL-D), 16.5 (EPAC-D), and 11.6 m s^{-1} (IPAC-D). Annotation denotes the implied "steering level" of the waves (indicated by the asterisk), together with the peak altitudes of the net Kelvin-mode energy sources: H_K and P_K (green and red lines, respectively), as seen in the control simulation (Figure 7a).

eddy contribution can be found in the composite picture of Figure 15c, which shows that the accompanying Rossby wave train in this case is slightly weaker in amplitude, in addition to being less trapped in the key subtropical belt 15°–20°. The reason for this reduced trapping is not clear, but may be tied to the faster propagation speed of the waves at roughly 17 versus 11 m s^{-1}, which ultimately sets the speed of the disturbance's associated Rossby wave source.

To explain the increase in Kelvin wave propagation speed, Figure 16 compares the vertical profiles of the climatological zonal wind near the equator in these two cases (as well as in IPAC-D), where different offsets have been added to allow comparison of the mean flow in the wave's moving frame of reference (see the figure caption for details). The comparison shows the waves to have a well-defined "steering level" at around 325 hPa or roughly 9.1 km, corresponding to an intrinsic wave propagation speed of around 17 m s^{-1}. This estimate, though empirical, is considered to be reliable for two reasons, both of which point to the $n = 3$ mode as being critical to the wave's propagation, despite the energetic dominance of the $n = 1$ mode. The first is that the implied steering level of the waves, as indicated by the green line in Figure 16, is almost perfectly coincident with the peak altitude of the net tropical heating source H_K (whose dominant contribution is from the $n = 3$ mode; see Figure 7), while lying several kilometers below that of the remote eddy source P_K. The second is that the intrinsic propagation speed of the waves is very close to that of the $n = 3$ mode (i.e., 16.9 vs. 17.5 m s^{-1}, respectively), where the latter was derived in a completely independent fashion based on a *dry* linear model calculation. Given this correspondence, it is suggested that the $n = 3$ mode may actually play a primary role in setting the propagation speed of the waves, as opposed to the $n = 1$ mode, in agreement with previous modeling work by Tulich et al. (2007) and Tulich and Mapes (2008).

5.3. Effects of Midlatitude Eddy Damping Under the IPAC Basic State

Turning finally to the effects of eddy damping under the easterly sheared IPAC basic state (IPAC-D), Figure 17a reveals an eastward-moving tropical wave spectrum that is now dominated not only by the signals of high-frequency Kelvin waves, but also those of the model's lower-frequency MJO. This result shows that external forcing from the midlatitudes is not essential for either of these two distinct modes of variability, in accordance with MK16. At the same time, however, the dearth of power at frequencies and zonal wavenumbers between these two modes is evidence once again that such forcing is nevertheless critical for driving the intermediate band of slow-moving dispersive Kelvin-like signals, in addition to amplifying the signals of the simulated MJO (compare Figure 17a vs. Figure 9a). Additional evidence of an important supporting role of the midlatitudes in forcing the MJO can be found in a modeling study by Hall et al. (2017).

Considering the net modal energetics of the simulated MJO, Figure 17b shows that the disturbance is primarily driven by the $n = 1$ tropical heating source H_{K1}, with an important secondary contribution from the $n = 1$ remote eddy source. Inspection of Figure 17c shows that the mechanism of this internal eddy feedback is essentially the same as discussed previously, but where the associated flanking Rossby gyres have shallower northwest-southeast tilts, implying predominantly poleward propagation of Rossby wave energy. Overall, the pattern looks very similar to that obtained in idealized simulations of the remote response to a prescribed MJO-like heat source, described in Monteiro et al. (2014, see their Figure 2c). Results confirming that these Rossby gyres indeed act to strengthen the model's MJO analog, in addition to its higher-frequency Kelvin waves, are contained in Figure 18, which shows how the rain signals of both wave types are reduced in response to weakening of the subtropical jet, through a reduced contribution of the remote eddy source P_{K1} (see the inset in Figure 18b).
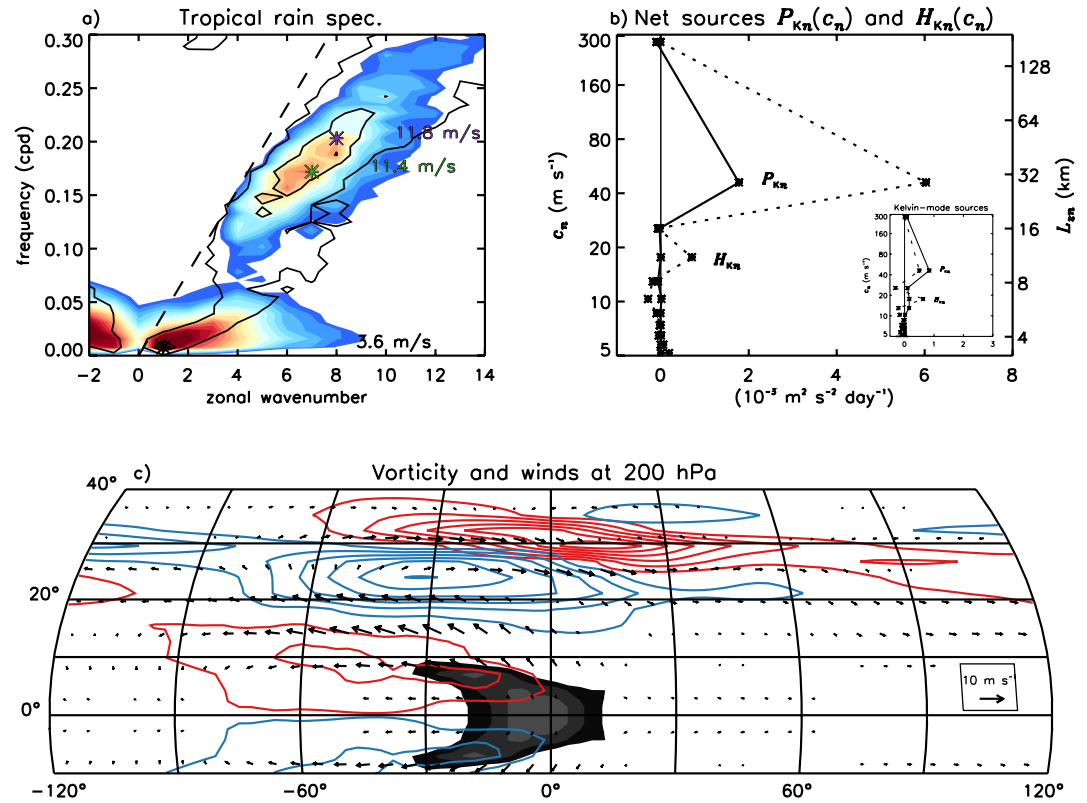
Figure 17. Similar to Figure 15, but for the eddy-damped variant of the standard IPAC integration (IPAC-D), where the net modal energetics in panel (b) and the composite picture in panel (c) is for the model's MJO analog. For completeness, the inset in panel (b) shows the net modal energetics of the higher-frequency Kelvin wave signals with periods less than 30 days. The composite structure of the simulated MJO was calculated using the same approach as in Appendix D.
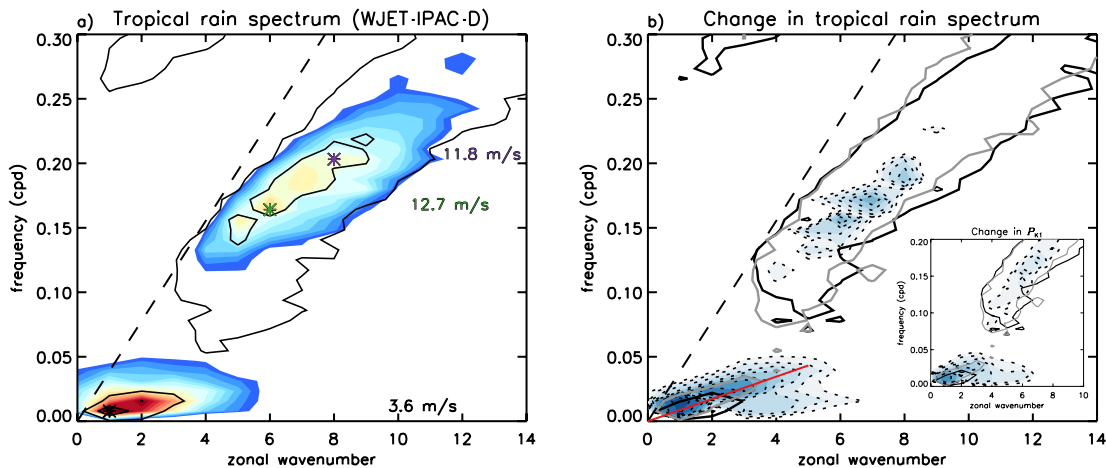

Figure 18. (a) Similar to Figure 17a, but for the eddy-damped variant of the weak-jet IPAC integration (WJET-IPAC-D). (b) Change in the tropical rain spectrum (WJET-IPAC-D minus IPAC-D), where the plotting convention is the same as in Figure 12a, except for the additional annotation showing a Kelvin wave phase speed of 4 m s^{-1} (red line), to highlight the preferential weakening of the simulated MJO's slow-moving Kelvin-mode signals in tropical rain. Inset in panel (b) shows how this weakening, in addition that of the higher-frequency Kelvin waves, is associated with reduction in the $n = 1$ remote eddy source P_{Kl}, following the same plotting convention as in Figure 12e.

6. Summary and Concluding Remarks

This study employed a global model with superparameterized physics to address the problem of moist tropical waves and their dependence on the basic state, with an emphasis on two forms of eastward-moving tropical wave variability: Kelvin waves and the MJO. The primary goal was to shed light on the observed regionality of these two wave types (as quantified in Figure 1), which has yet to be fully explained. Results from a series of aquaplanet simulations and analyses support the hypothesis that regional variations of the background zonal flow $\bar{u}$ are of leading importance, owing to their mediating influence on at least two different mechanistic pathways, in addition to Doppler-shifting effects. Brief sketches of these two affected pathways, encapsulating the main findings of this study, are discussed below.

The first pathway involves the forcing of equatorially trapped Kelvin-mode circulations by eastward and equatorward-propagating Rossby-type eddies impinging on the tropics from higher latitudes. The forcing is thought to arise as the eddies encounter a critical latitude where their zonal phase speed matches the background zonal flow (i.e., $U - c = 0$). Despite being confined to the subtropical upper troposphere, the primary effect of the eddy forcing is to excite and maintain deep overturning Kelvin-mode circulations in the tropical troposphere that are manifested in spectral space by eastward-propagating signals in tropical rainfall. The spectral structure of these signals is similar to that of their parent eddies, whose dispersion is well explained by the linear Rossby wave theory. Because eddies are absorbed where $U - c = 0$, the spectrum of forced rain signals is seen to depend crucially on $\bar{u}$, and especially the strength of the subtropical jet. This spectrum of forced variability includes not only slower-moving, dispersive signals inherited from the storm tracks, but also faster-moving, non-dispersive signals that are regarded as traditional free Kelvin waves. Rather than being set by the forcing, however, the phase speed of these free waves appears to be set by the "dry" speed of the $n = 3$ vertical mode of the troposphere, modified by Doppler shifting at a steering level in the upper troposphere at around 9 km.

The second pathway lies in the lower free troposphere. Intraseasonal fluctuations in Kelvin-mode zonal wind modulate the activity of higher-frequency equatorial Rossby-type eddies (referred to here as "shear-induced eddy modulation" or SIEM), in such a way as to promote the slow eastward propagation of moisture anomalies near the equator. While the importance of this modulation toward MJO propagation is generally accepted, here its efficacy was seen to be directly tied to the strength of the background cyclonic shear on the flanks of the simulated ITCZ. This mean-flow dependence of the SIEM mechanism appears to lie at the heart of the explanation for why the MJO's convective signals in nature tend to be confined mainly to the tropical Indo-Pacific (where low-level westerlies are the norm and the associated flanking belts of mean cyclonic shear are generally larger than elsewhere). A further reason is evidently tied to the modulating effects of the background zonal flow at upper levels. In particular, results showed how the presence of strong upper-level mean easterlies in the tropics, together with a strong subtropical jet (as is typical of the Indo-Pacific sector, especially during the solstice seasons) tends to be optimal for the MJO, not only by insulating the disturbance from the effects of relatively fast-moving eddies in the extratropics (that otherwise tend to excite higher-frequency Kelvin waves), but also by fostering positive eddy-momentum feedbacks involving the disturbance's associated flanking Rossby gyres.

Many of the above findings are novel, with very little in the way of theoretical guidance. It thus remains unclear as to how profound (or secondary) these upper-level flanking Rossby gyres are to the dynamics of either Kelvin waves or the MJO. Another important question concerns the underlying causes for the mean-flow dependence of the SIEM mechanism, which has only recently been hinted at through careful processing of model reanalysis data (Wang et al., 2019). Finally, there is a need to understand how the SIEM mechanism is affected not only by the background zonal flow structure, but also by the distributions of time-mean convective heating and moisture, all of which are shaped by the time-mean SST field. Investigation of this issue might ultimately help to explain why the MJO tends to be strongest during boreal winter, despite the fact that low-level mean westerlies over the tropical Indo-Pacific tend to be strongest during boreal summer (Zhang & Dong, 2004).

Future work should try to reduce this study's main limitations. The approach of using a global model with axisymmetric forcing and lower boundary conditions to study the regionality of moist tropical waves, while convenient for isolating the effects of different local basic states, leaves open questions about the effects of

zonal gradients in the basic state. For example, there is some evidence to suggest that zonal gradients in mean-state moisture over the Indian Ocean may also be important for explaining the observed regionality of the MJO (Hsu & Li, 2012; Liu & Wang, 2016; Sobel & Maloney, 2013; Sukhatme, 2014). Meanwhile, the set-up used here precludes the possibility of any sort of regionality driven by (stationary) interactions between different parts of the tropics, through Rossby wave teleconnections (Matthews & Kiladis, 1999). Despite these limitations, it appears going forward that an expanded view of the spectrum of eastward-moving tropical wave variability in nature may be needed, encompassing both the tropics and extratropics as a tightly coupled dynamical system.

Appendix A: CRM Orientation as a Random Walk

The choice of 2D-CRM orientation is essentially arbitrary in the context of the standard method of SP, since the real atmosphere never behaves in a strictly 2D fashion. While most studies have chosen to adopt a fixed orientation, the approach here is to introduce a variable orientation angle β, where the latter is treated in a random, as opposed to deterministic, fashion. The intent is to eliminate the otherwise biased sampling of one horizontal direction over all others. The expression for β at time level $n + 1$ of the large-scale host model is given by:

$$\beta_{n+1} = \beta_n + \theta^* z_n, \tag{A1}$$

where z_n in a normally distributed random variable with zero mean and a standard deviation of unity, and θ^* is an arbitrary scaling parameter. The latter is chosen so that the root-mean-square of the net change in β per day is π radians.

The above strategy is quite different from that originally implemented in the SP-WRF, where β was chosen to match the direction of the large-scale horizontal wind at low levels, following the suggestion of Grabowski (2004). To assess the impact of this revision, the model was used to perform a series of real-world seasonal climate integrations, following the protocol outlined in Section 5 of T15. Results in Figures A1 and A2 show that the impact in terms of the simulated time-mean climate is generally quite small. The only significant difference is a slight improvement in the correlation between the simulated versus observed spatial patterns of the u-wind and v-wind components, both near the surface and at 200 hPa (see Figure A2).

This insensitivity is also seen when comparing the simulated versus observed space-time spectra of tropical rain, depicted in Figure A3. The model spectra appear broadly similar, with only modest differences pointing to either slightly weaker Kelvin and tropical depression-type disturbances, or slightly stronger westward-moving inertia-gravity waves, leading to marginally better agreement with observations. The reason(s) for these differences, in addition to those seen in Figure A2, is not clear but may be due to changes in the parameterized CMT, via changes in the statistical sampling of the two large-scale horizontal wind components. Regardless, such improvements are welcome and provide justification for the revised approach, in addition to its intended purpose of ensuring all directions are treated equally in a statistical sense.

The conclusion that the model performance is largely insensitive to the choice of CRM orientation is somewhat different from that of T15, which examined the effects of aligning the CRMs everywhere perpendicular, as opposed to parallel, to the large-scale horizontal flow at low levels, except in regions of strong convection. The focus in that study, however, was on the simulated time-mean pattern of surface rain, where regional differences exceeding 3 mm dy^{-1} (in an absolute sense) were reported to be statistically significant at the 80% confidence interval, which is lower than the 90% interval used here. Another important distinction is that the model performance documented in Figures A1–A3 is significantly better than that seen in T15′s Figures 10, 12a and 14, respectively. The reason is due mainly to the correction of a coding error involving the specified surface albedo, which was inadvertently set to zero over all non-glaciated land points, in addition to the use of a different radiation scheme and some tuning/modification to the TKE-based turbulent mixing scheme.
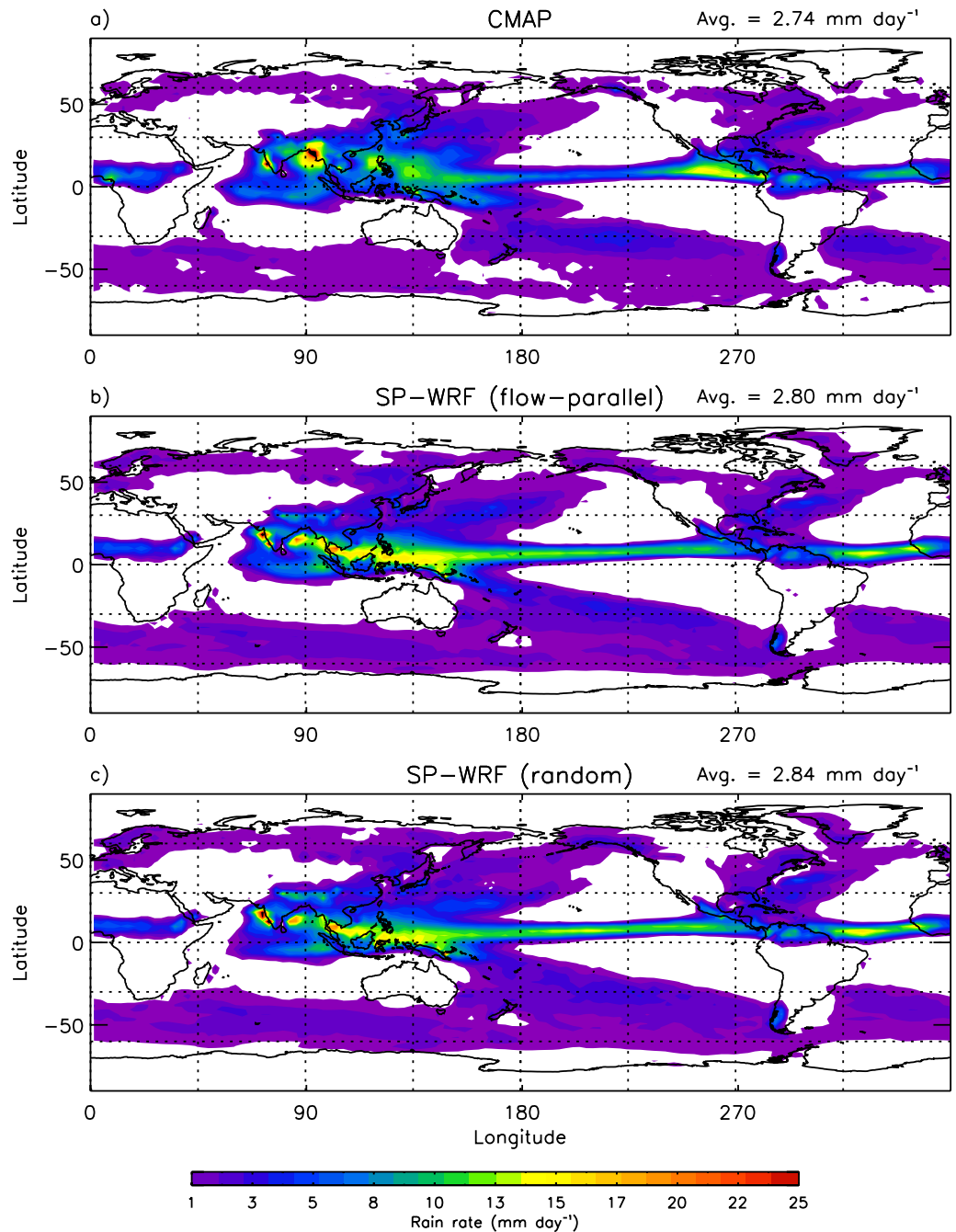
Figure A1. Impact of replacing the original flow-parallel CRM orientation strategy in the SP-WRF with a newly devised random approach, in terms of the simulated time-mean pattern of surface rain for the period June–August 2008–2012. Observations in panel (a) were taken from the Climate Prediction Center's Merged Analysis of Precipitation (CMAP; Xie & Arkin, 1997). Model results in panels (b) and (c) are for the flow-parallel versus random orientation strategies, respectively. Based on a Student's *t*-test, the null hypothesis that the two simulations are statistically identical cannot be rejected anywhere using a 90% confidence level or above.

Figure A2. Taylor diagram for SP-WRF seasonal climate integrations performed using either the original flow-parallel or newly devised random CRM orientation strategies described in the text (red vs. green symbols, respectively). Symbols with annotation denote the surface rainfall (R), ocean-masked precipitable water (PW), outgoing longwave radiation (OLR), and zonal/meridional wind components at both 10 m and 200 hPa (U10/V10 and U200/V200, respectively). Results were obtained using the same observational datasets as described in Section 5 of T15.

Appendix B: Horizontal Spectral Analysis of the Simulated Vorticity

As shown in Figure 4, the dispersive propagation of the model's extratropical wave signals is well captured by that theoretically expected for non-divergent Rossby waves on the sphere, with implied meridional wavenumbers   in the range 0–9. To address whether these implied values of   are actually prominent in the control simulation, a horizontal spectral analysis of high-pass-filtered (<120 days) $\zeta 200$ anomalies was performed, where the data were first horizontally interpolated from the model's rectangular latitude-longitude grid to a square Mercator grid with a uniform grid spacing of roughly 300 km in both directions. Also, to asses how eddy structures differ in the "upper" versus "lower" midlatitudes, a windowing function was used to isolate anomaly patterns in the approximate latitude belts of either: (a) 45°–70° or (b) 20°–45°, respectively.

Figure B1 depicts the resulting time-averaged horizontal (k-l) wavenumber spectra, where the coefficients for positive and negative wavenumbers have been averaged together to identify the dominant scales of variability. Consistent with the picture implied by the dispersion curves in Figure 4a, the spectrum for the upper midlatitude belt (Figure B1a) shows that the dominant eddies in this region tend to have a peak meridional wavenumber l_{max} near zero, except at $k = 1$ and 2, where $l_{max} = 5$ and 4, respectively. The story is much the same for the lower midlatitude belt (compare Figures B1b and 4b), but where $l_{max} = 9$ for $k = 1$–3 and then decreases to 7 for the dominant synoptic-scale eddies at $k = 4$ and 5, before dropping off sharply from 5 to 0 at $k = 7$ and 8, respectively. Overall, these results are supportive of the use of linear Rossby wave theory, in the form of Equation 6, to explain the propagation and dispersion of the model's storm track disturbances, with the steering level of the waves implied a posteriori to lie at around 300 hPa.
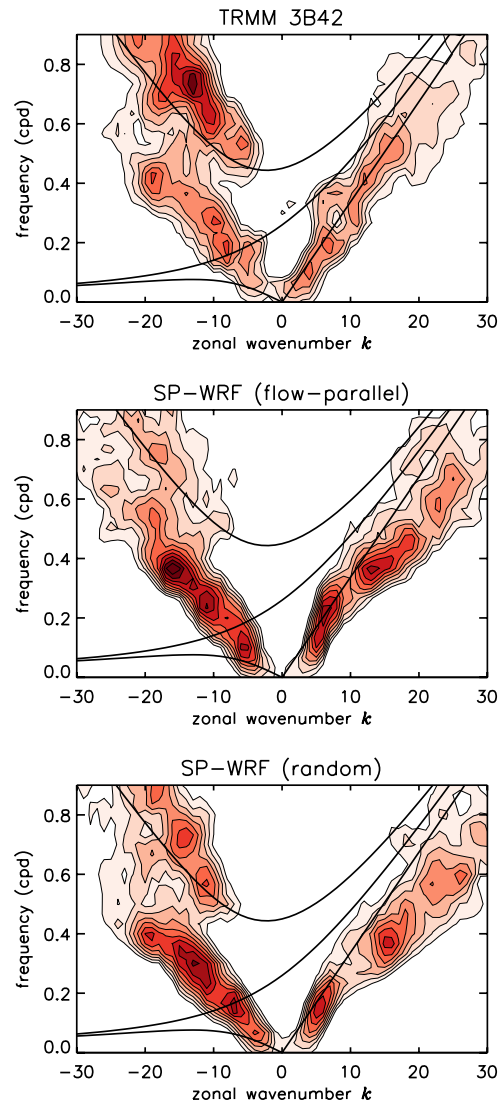
Observed vs simulated rain spectrum (15°S–15°N)

Figure A3. Similar to Figure A1 but for the average global space-time spectrum of tropical rain. Results were obtained using the same methods (and observational data) as in Figure 1, except that no regional tapering was applied and the time window was reduced from 96 to 30 days, due to the smaller data record. Shading with contours denote where the signal-to-noise ratio ≥ 1.05, with intervals of 0.05. Solid curves denote the dispersion relations of various dry equatorial wave modes with equivalent depth of 25 m.

Appendix C: Determination of the Trapping Scale ϕ_*

The trapping scale ϕ_* is a theoretical parameter that determines the degree to which (dry) linear equatorial waves of a given equivalent depth h_0 (or alternatively, Kelvin/gravity wave speed c_*) are trapped near the equator (Gill, 1980). To arrive at an appropriate value of ϕ_* for the SP-WRF's simulated moist eastward-moving tropical wave disturbances, the model output from the control simulation was first spectrally filtered to retain eastward-moving zonal wavenumbers in the range $k = 1$–14 and periods in the range 2–120 days. Next, a principal component (PC/EOF) analysis was applied to the combined fields of daily averaged precipitation and the divergent component of the 200-hPa zonal wind $U_{\chi 200}$, both normalized to have a standard deviation of unity, where the structural dimension of the analysis
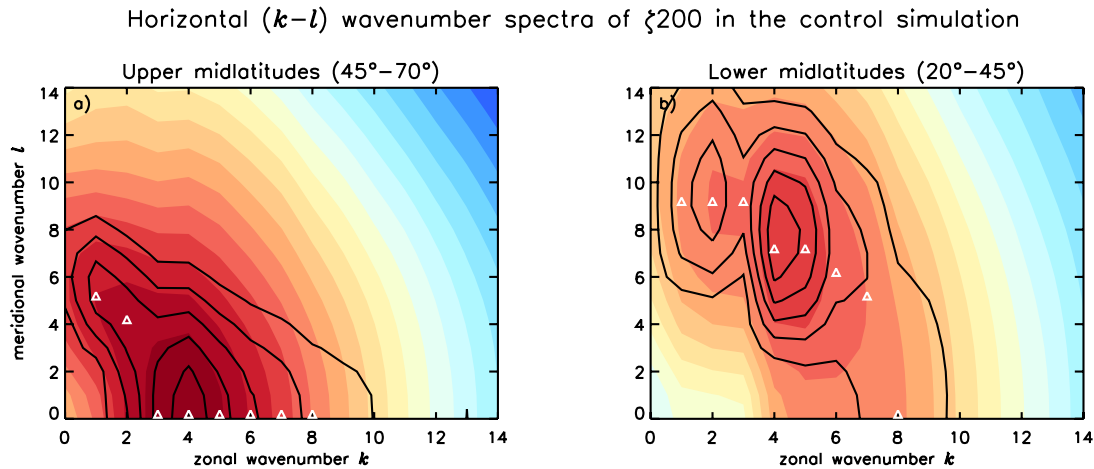
Horizontal $(k-l)$ wavenumber spectra of $\zeta200$ in the control simulation

Figure B1. Time-averaged horizontal wavenumber (k-) spectra of $\zeta200$ for latitudes in the range: (a) 45°–70° and (b) 20°–45°. Shading denotes the logarithm of the raw power, while contours denote the ratio of the raw power to a smoothed background, with levels starting at 1.1 and intervals of 0.2. Symbols denote peak values of   (in terms of raw power) for different values k in the range 1–8, where the vertical position of each symbol is slightly offset from its actual position for plotting purposes.

was latitude in the range 30°N–30°S, while the sampling dimension was longitude together with time. The resulting global regressed structures of the leading PC, denoted PC1, are indicated by the solid curves in Figure C1a, where the percentage of the total filtered variance explained by the PC is around 38%. Note that this percentage increases to 85% when the analysis is restricted to $U_{\chi200}$, with very little change in the associated eigenstructure (results not shown). As indicated by the black dotted curve in Figure C1a, the regressed structure of $U_{\chi200}$ is well captured by that theoretically expected for dry Kelvin waves with a trapping scale $\phi_0 \approx 9°$, corresponding to a dry Kelvin/gravity wave speed $c_* \approx 45\,\mathrm{m\,s^{-1}}$. The implication is that eddy momentum forcing in the subtropics can indeed potentially act to excite the simulated moist Kelvin waves, despite the relatively narrow structure of their associated precipitation anomalies. Comparison of the gray solid and dotted curves in Figure C1a shows that the latter have an estimated trapping scale $\phi_* \approx 3°$, which is presumably set by the width of the model's time-mean tropical rain band (see Figure 2b).

To assess the realism of the above picture, a similar PC/EOF analysis was applied to TRMM rainfall data combined with ERA5 (Hersbach et al., 2020) estimates of $U_{\chi200}$ for the period 1998–2017. Preparation of the data involved removing the first three harmonics of the seasonal cycle, as well as horizontal coarse graining to achieve a spatial resolution comparable to that of the SP-WRF (i.e., 2.5° vs. 2.8°). Also, due to the broader diversity of tropical wave types in the real world as compared to the control simulation, the latitude range of the analysis was restricted to within ± 10° of the equator, while the spectral filter was revised to match that devised for isolating moist Kelvin wave signals by Kiladis et al. (2009; see their Figure 1). The leading PC structures obtained under these modifications, depicted in Figure C1b, are very similar to those obtained for the model, but where the implied values of ϕ_* are roughly 2° larger in both cases. Meanwhile, repeating the analysis for MJO-filtered anomalies, using the same filter as in Wheeler and Kiladis (1999), yields an even broader zonal wind structure ($\phi_* \approx 17°$), while the precipitation structure appears more like that in Figure C1a, but with substantial negative side lobes (results not shown). In summary, it appears that the potential for extratropical forcing of eastward-moving moist tropical variability, via the projection pathway of Hoskins and Yang (2000), is substantial in both the real world and the aquaplanet setup considered herein.
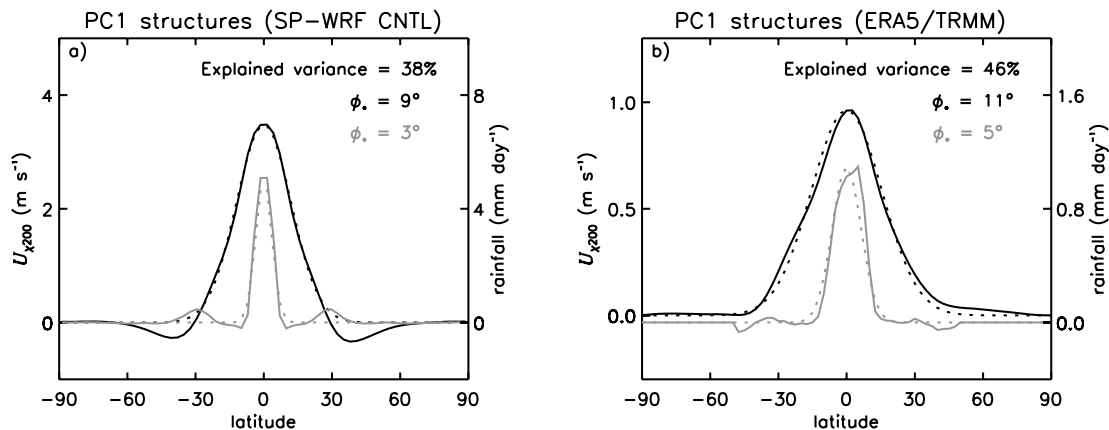
Figure C1. (a) SP-WRF simulated versus (b) observed leading meridional PC structures (obtained via linear regression) of Kelvin-filtered anomaly patterns in precipitation (solid gray) together with the divergent component of the 200-hPa zonal wind ($U_{\chi 200}$; solid black). Dotted curves denote a least-squares fit of the data to the theoretical eigenstructure of a (dry) linear Kelvin wave with the annotated trapping scale ϕ_* as the fitting parameter. Results in panel (a) are based on the control aquaplanet simulation detailed in Section 2. Details about the methods used to obtain the PCs can be found in the text.

Appendix D: Composite Structures of the Model's MJO Analog

As discussed in Section 4, the tropical rain spectrum produced in the standard IPAC case (Figure 9a) is dominated by a pronounced MJO-like spectral peak at $k = 2$, closely matching the corresponding observed spectrum in Figure 1a. To further assess the realism of this simulated disturbance, a composite analysis was performed in physical space using the same basic methodology as for the Kelvin wave composite in Figure 5, but with the object-defining filter specified to retain only zonal wavenumbers in the range $k = 1$–5 and periods in the range 30–120 days. The resulting horizontal flow and streamfunction anomaly patterns at 200 and 850 hPa are plotted in Figures D1a and D1b, respectively. The familiar quadrapole gyre patterns are readily apparent in both cases, with the centers of the dominant gyres located at around 25° latitude in the upper panel, compared to around 10° in the lower one, broadly similar to what is observed in the context of the real-world MJO (e.g., see Figure 2 in Kiladis et al., 2005). Taking the latter observational study as a benchmark, however, it is evident that the simulated equatorial zonal wind anomalies at 850 hPa are too strong by roughly a factor of 2, an error that is interpreted to stem from an overly strong Kelvin-mode circulation component in the model. This interpretation is based on the fact that the amplitude of the simulated streamfunction anomalies is comparable to what is actually observed. Despite this discrepancy, it is clear that the simulated disturbance is more than just a pure Kelvin wave, since the low-level westerlies trailing its convection center at the equator are substantially stronger than the low-level easterlies out ahead, as part of an associated "westerly wind burst" (WWB)—a tell-tale feature of the MJO. The accompanying "swallowtail" pattern in the simulated rainfall anomalies is also reminiscent of that seen in observations (Adames & Wallace, 2014b; Zhang & Ling, 2012). Looking at longitude-height cross-sections of the disturbance at the equator, Figures D1c and D1d reveal several additional similarities to the observed MJO, including tilted structures in temperature T, specific humidity q_v, and apparent heating Q anomalies that imply a gradual deepening of moisture and convection as the precipitating phase of the disturbance arrives at a fixed point from the west. Particularly noteworthy in this regard is the fact that fluctuations in q_v in the middle troposphere are roughly an order of magnitude larger (in moist static energy units) than those in T, which is unlike what is seen in convectively coupled Kelvin waves, where fluctuations in q_v and T are more comparable (Straub & Kiladis, 2003a). In summary, it appears that the MJO-like mode of variability produced in the model can indeed be considered as analog of the real MJO.
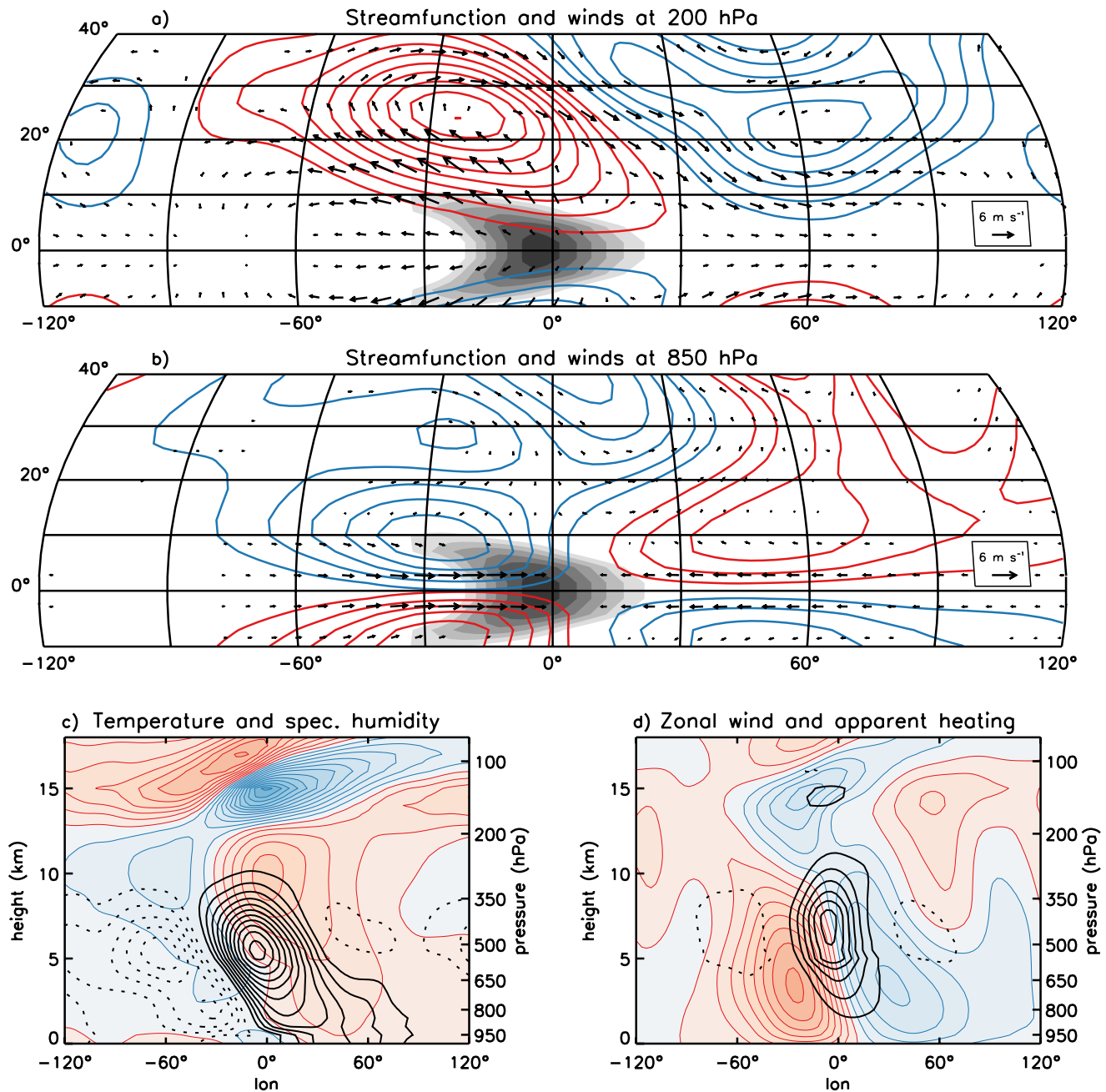
Figure D1. Composite dynamical structures of the simulated MJO-like disturbance produced in the standard IPAC integration. (a) and (b) Anomalous horizontal flow vectors and streamfunction at 200 and 850 hPa, respectively, where red/blue contours denote positive/negative streamfunction anomalies with an interval of (a) 5×10^5 and (b) $1 \times 10^6\ \text{m}^2\ \text{s}^{-1}$ (c) Longitude-height cross-section of temperature (shading) and specific humidity anomalies (black contours) at the equator, with both fields plotted in temperature units at an interval of 0.2K; red/blue shading and solid/dotted black contours denote positive/negative values. (d) Similar to panel (c), but for zonal wind (shading) and apparent heating (black contours), with contour intervals of 1 m s^{-1} and 1K day^{-1}, respectively.

Data Availability Statement

All data for the SP-WRF simulations and analyses described in this study are available at https://downloads. psl.noaa.gov/Projects/FAIR_paper_data/20210302_01/.

References

Adames, Á. F., & Kim, D. (2015). The MJO as a dispersive, convectively coupled moisture wave: Theory and observations. *Journal of the Atmospheric Sciences*, *73*(3), 913–941. https://doi.org/10.1175/JAS-D-15-0170.1

Adames, Á. F., Patoux, J., & Foster, R. C. (2014). The contribution of extratropical waves to the MJO wind field. *Journal of the Atmospheric Sciences*, *71*(1), 155–176. https://doi.org/10.1175/JAS-D-13-084.1

Adames, Á. F., & Wallace, J. M. (2014a). Three-dimensional structure and evolution of the MJO and its relation to the mean flow. *Journal of the Atmospheric Sciences*, *71*(6), 2007–2026. https://doi.org/10.1175/JAS-D-13-0254.1

Adames, Á. F., & Wallace, J. M. (2014b). Three-dimensional structure and evolution of the vertical velocity and divergence fields in the MJO. *Journal of the Atmospheric Sciences*, *71*(12), 4661–4681. https://doi.org/10.1175/JAS-D-14-0091.1

Andersen, J. A., & Kuang, Z. (2012). Moist static energy budget of MJO-like disturbances in the atmosphere of a zonally symmetric aquaplanet. *Journal of Climate*, *25*(8), 2782–2804. https://doi.org/10.1175/JCLI-D-11-00168.1

Arnold, N. P., Kuang, Z., & Tziperman, E. (2013). Enhanced MJO-like variability at high SST. *Journal of Climate*, *26*(3), 988–1001. https://doi.org/10.1175/JCLI-D-12-00272.1

Arnold, N. P., & Randall, D. A. (2015). Global-scale convective aggregation: Implications for the Madden-Julian Oscillation. *Journal of Advances in Modeling Earth Systems*, *7*(4), 1499–1518. https://doi.org/10.1002/2015MS000498

Benedict, J. J., & Randall, D. A. (2011). Impacts of idealized air-sea coupling on Madden-Julian Oscillation structure in the superparameterized CAM. *Journal of the Atmospheric Sciences*, *68*(9), 1990–2008. https://doi.org/10.1175/JAS-D-11-04.1

Bennet, J. R., & Young, J. A. (1971). The influence of latitudinal wind shear upon large-scale wave propagation into the tropics. *Monthly Weather Review*, *99*(3), 202–214. https://doi.org/10.1175/1520-0493(1971)099<0202:TIOLWS>2.3.CO;2

Chao, W. C., & Lin, S.-J. (1994). Tropical intraseasonal oscillation, super cloud clusters, and cumulus convection schemes. *Journal of the Atmospheric Sciences*, *51*(10), 1282–1297. https://doi.org/10.1175/1520-0469(1994)051<1282:TIOSCC>2.0.CO;2

Chikira, M. (2014). Eastward-propagating intraseasonal oscillation represented by Chikira-Sugiyama cumulus parameterization. Part II: Understanding moisture variation under weak temperature gradient balance. *Journal of the Atmospheric Sciences*, *71*(2), 615–639. https://doi.org/10.1175/JAS-D-13-038.1

Das, S., Sengupta, D., Chakraborty, A., Sukhatme, J., & Murtugudde, R. (2016). Low-frequency intraseasonal variability in a zonally symmetric aquaplanet model. *Meteorology and Atmospheric Physics*, *128*(6), 697–713. https://doi.org/10.1007/s00703-016-0448-y

Dee, D. P., Uppala, S. M., Simmons, A. J., Berrisford, P., Poli, P., Kobayashi, S., et al. (2011). The ERA-Interim reanalysis: Configuration and performance of the data assimilation system. *Quarterly Journal of the Royal Meteorological Society*, *137*(656), 553–597. https://doi.org/10.1002/qj.828

DeMott, C. A., Stan, C., & Randall, D. A. (2013). Northward propagation mechanisms of the Boreal Summer Intraseasonal Oscillation in the ERA-Interim and SP-CCSM. *Journal of Climate*, *26*(6), 1973–1992. https://doi.org/10.1175/JCLI-D-12-00191.1

Dias, J., & Kiladis, G. N. (2014). Influence of the basic state zonal flow on convectively coupled equatorial waves. *Geophysical Research Letters*, *41*(19), 6904–6913. https://doi.org/10.1002/2014GL061476

Emanuel, K. A. (1987). An air-sea interaction model of intraseasonal oscillations in the tropics. *Journal of the Atmospheric Sciences*, *44*, 2324–2340.

Fuchs, Ž., & Raymond, D. J. (2017). A simple model of intraseasonal oscillations. *Journal of Advances in Modeling Earth Systems*, *9*(2), 1195–1211. https://doi.org/10.1002/2017MS000963

Fulton, S. R., & Schubert, W. H. (1985). Vertical normal mode transforms: Theory and application. *Monthly Weather Review*, *113*, 647–658.

Gehne, M., & Kleeman, R. (2012). Spectral analysis of tropical atmospheric dynamical variables using a linear shallow-water modal decomposition. *Journal of the Atmospheric Sciences*, *69*(7), 2300–2316. https://doi.org/10.1175/JAS-D-10-05008.1

Gill, A. E. (1980). Some simple solutions for heat-induced tropical circulation. *Quarterly Journal of the Royal Meteorological Society*, *106*(449), 447–462. https://doi.org/10.1002/qj.49710644905

Grabowski, W. W. (2003). MJO-like coherent structures: Sensitivity simulations using the Cloud-Resolving Convection Parameterization (CRCP). *Journal of the Atmospheric Sciences*, *60*(6), 847–864. https://doi.org/10.1175/1520-0469(2003)060<0847:MLCSSS>2.0.CO;2

Grabowski, W. W. (2004). An improved framework for superparameterization. *Journal of the Atmospheric Sciences*, *61*(15), 1940–1952. https://doi.org/10.1175/1520-0469(2004)061<1940:AIFFS>2.0.CO;2

Grabowski, W. W., & Smolarkiewicz, P. K. (1999). CRCP: A cloud resolving convection parameterization for modeling the tropical convecting atmosphere. *Physica D: Nonlinear Phenomena*, *133*(1), 171–178. https://doi.org/10.1016/S0167-2789(99)00104-9

Hall, N. M. J., Thibaut, S., & Marchesiello, P. (2017). Impact of the observed extratropics on climatological simulations of the MJO in a tropical channel model. *Climate Dynamics*, *48*(7), 2541–2555. https://doi.org/10.1007/s00382-016-3221-5

Hannah, W. M., Jones, C. R., Hillman, B. R., Norman, M. R., Bader, D. C., Taylor, M. A., et al. (2020). Initial results from the super-parameterized E3SM. *Journal of Advances in Modeling Earth Systems*, *12*(1), e2019MS001863. https://doi.org/10.1029/2019MS001863

Hayashi, Y., & Golder, D. G. (1977). Space-time spectral analysis of mid-latitude disturbances appearing in a GFDL general circulation model. *Journal of the Atmospheric Sciences*, *34*(2), 237–262. https://doi.org/10.1175/1520-0469(1977)034<0237:STSAOM>2.0.CO;2

Hendon, H. H., & Salby, M. L. (1994). The life cycle of the Madden-Julian Oscillation. *Journal of the Atmospheric Sciences*, *51*(15), 2225–2237. https://doi.org/10.1175/1520-0469(1994)051<2225:TLCOTM>2.0.CO;2

Hersbach, H., Bell, B., Berrisford, P., Hirahara, S., Horányi, A., Muñoz-Sabater, J., et al. (2020). The ERA5 global reanalysis. *Quarterly Journal of the Royal Meteorological Society*, *146*(730), 1999–2049. https://doi.org/10.1002/qj.3803

Hoskins, B. J., & Karoly, D. J. (1981). The steady linear response of a spherical atmosphere to thermal and orographic forcing. *Journal of the Atmospheric Sciences*, *38*(6), 1179–1196. https://doi.org/10.1175/1520-0469(1981)038<1179:TSLROA>2.0.CO;2

Hoskins, B. J., & Yang, G.-Y. (2000). The equatorial response to higher-latitude forcing. *Journal of the Atmospheric Sciences*, *57*(9), 1197–1213. https://doi.org/10.1175/1520-0469(2000)057<1197:TERTHL>2.0.CO;2

Hsu, H.-H., Hoskins, B. J., & Jin, F.-F. (1990). The 1985/86 intraseasonal oscillation and the role of the extratropics. *Journal of the Atmospheric Sciences*, *47*(7), 823–839. https://doi.org/10.1175/1520-0469(1990)047<0823:TIOATR>2.0.CO;2

Hsu, P.-C., & Li, T. (2012). Role of the boundary layer moisture asymmetry in causing the eastward propagation of the Madden-Julian Oscillation. *Journal of Climate*, *25*(14), 4914–4931. https://doi.org/10.1175/JCLI-D-11-00310.1

Huaman, L., Schumacher, C., & Kiladis, G. N. (2020). Eastward-propagating disturbances in the tropical Pacific. *Monthly Weather Review*, *148*(9), 3713–3728. https://doi.org/10.1175/MWR-D-20-0029.1

Huffman, G. J., Adler, R. F., Bolvin, D. T., Gu, G., Nelkin, E. J., Bowman, K. P., et al. (2007). The TRMM Multisatellite Precipitation Analysis (TMPA): Quasi-global, multiyear, combined-sensor precipitation estimates at fine scale. *Journal of Hydrometeorology*, *8*, 38–55.

Iacono, M. J., Delamere, J. S., Mlawer, E. J., Shephard, M. W., Clough, S. A., & Collins, W. D. (2008). Radiative forcing by long-lived greenhouse gases: Calculations with the AER radiative transfer models. *Journal of Geophysical Research: Atmospheres*, *113*(D13). https://doi.org/10.1029/2008JD009944

Jiang, X., Maloney, E., & Su, H. (2020). Large-scale controls of propagation of the Madden-Julian Oscillation. *npj Climate and Atmospheric Science*, *3*(1), 29. https://doi.org/10.1038/s41612-020-00134-x

Kang, I.-S., Liu, F., Ahn, M.-S., Yang, Y.-M., & Wang, B. (2013). The role of SST structure in convectively coupled Kelvin-Rossby waves and its implications for MJO formation. *Journal of Climate*, *26*(16), 5915–5930. https://doi.org/10.1175/JCLI-D-12-00303.1

Khairoutdinov, M. F., & Emanuel, K. (2018). Intraseasonal variability in a cloud-permitting near-global equatorial aquaplanet model. *Journal of the Atmospheric Sciences*, *75*(12), 4337–4355. https://doi.org/10.1175/JAS-D-18-0152.1

Kiladis, G. N., Straub, K. H., & Haertel, P. T. (2005). Zonal and vertical structure of the Madden-Julian oscillation. *Journal of the Atmospheric Sciences*, *62*(8), 2790–2809. https://doi.org/10.1175/JAS3520.1

Kiladis, G. N., Wheeler, M. C., Haertel, P. T., Straub, K. H., & Roundy, P. E. (2009). Convectively coupled equatorial waves. *Reviews of Geophysics*, *47*(2). https://doi.org/10.1029/2008RG000266

Kiranmayi, L., & Maloney, E. D. (2011). Intraseasonal moist static energy budget in reanalysis data. *Journal of Geophysical Research: Atmospheres*, *116*(D21). https://doi.org/10.1029/2011JD016031

Knutson, T. R., & Weickmann, K. M. (1987). 30–60 day atmospheric oscillations: Composite life cycles of convection and circulation anomalies. *Monthly Weather Review*, *115*(7), 1407–1436. https://doi.org/10.1175/1520-0493(1987)115<1407:DAOCLC>2.0.CO;2

Lee, M.-I., Kang, I.-S., & Mapes, B. E. (2003). Impacts of cumulus convection parameterization on aqua-planet AGCM simulations of tropical intraseasonal variability. *Journal of the Meteorological Society of Japan. Seres II*, *81*(5), 963–992. https://doi.org/10.2151/jmsj.81.963

Lee, S., & Held, I. M. (1993). Baroclinic wave packets in models and observations. *Journal of the Atmospheric Sciences*, *50*(10), 1413–1428. https://doi.org/10.1175/1520-0469(1993)050<1413:BWPIMA>2.0.CO;2

Lin, H., Brunet, G., & Derome, J. (2009). An observed connection between the North Atlantic Oscillation and the Madden-Julian Oscillation. *Journal of Climate*, *22*(2), 364–380. https://doi.org/10.1175/2008JCLI2515.1

Liu, F., & Wang, B. (2016). Role of horizontal advection of seasonal-mean moisture in the Madden-Julian Oscillation: A theoretical model analysis. *Journal of Climate*, *29*(17), 6277–6293. https://doi.org/10.1175/JCLI-D-16-0078.1

Ma, D., & Kuang, Z. (2016). A mechanism-denial study on the Madden-Julian Oscillation with reduced interference from mean state changes. *Geophysical Research Letters*, *43*(6), 2989–2997. https://doi.org/10.1002/2016GL067702

Maloney, E. D. (2009). The moist static energy budget of a composite tropical intraseasonal oscillation in a climate model. *Journal of Climate*, *22*(3), 711–729. https://doi.org/10.1175/2008JCLI2542.1

Maloney, E. D., & Dickinson, M. J. (2003). The intraseasonal oscillation and the energetics of summertime tropical western North Pacific synoptic-scale disturbances. *Journal of the Atmospheric Sciences*, *60*(17), 2153–2168. https://doi.org/10.1175/1520-0469(2003)060<2153:TIOATE>2.0.CO;2

Maloney, E. D., & Hartmann, D. L. (2001). The sensitivity of intraseasonal variability in the NCAR CCM3 to changes in convective parameterization. *Journal of Climate*, *14*(9), 2015–2034. https://doi.org/10.1175/1520-0442(2001)014<2015:TSOIVI>2.0.CO;2

Matthews, A. J., & Kiladis, G. N. (1999). The tropical-extratropical interaction between high-frequency transients and the Madden-Julian Oscillation. *Monthly Weather Review*, *127*(5), 661–677. https://doi.org/10.1175/1520-0493(1999)127<0661:TTEIBH>2.0.CO;2

Monteiro, J. M., Adames, Á. F., Wallace, J. M., & Sukhatme, J. S. (2014). Interpreting the upper level structure of the Madden-Julian oscillation. *Geophysical Research Letters*, *41*(24), 9158–9165. https://doi.org/10.1002/2014GL062518

Neale, R. B., & Hoskins, B. J. (2000). A standard test for AGCMs including their physical parametrizations: I: The proposal. *Atmospheric Science Letters*, *1*(2), 101–107. https://doi.org/10.1006/asle.2000.0022

Pratt, R. W. (1977). Space-time kinetic energy spectra in mid-latitudes. *Journal of the Atmospheric Sciences*, *34*(7), 1054–1057. https://doi.org/10.1175/1520-0469(1977)034<1054:STKESI>2.0.CO;2

Pritchard, M. S., Bretherton, C. S., & DeMott, C. A. (2014). Restricting 32–128 km horizontal scales hardly affects the MJO in the Superparameterized Community Atmosphere Model v.3.0 but the number of cloud-resolving grid columns constrains vertical mixing. *Journal of Advances in Modeling Earth Systems*, *6*(3), 723–739. https://doi.org/10.1002/2014MS000340

Randall, D., Khairoutdinov, M., Arakawa, A., & Grabowski, W. (2003). Breaking the cloud parameterization deadlock. *Bulletin of the American Meteorological Society*, *84*(11), 1547–1564. https://doi.org/10.1175/BAMS-84-11-1547

Randel, W. J., & Held, I. M. (1991). Phase speed spectra of transient eddy fluxes and critical layer absorption. *Journal of the Atmospheric Sciences*, *48*(5), 688–697. https://doi.org/10.1175/1520-0469(1991)048<0688:PSSOTE>2.0.CO;2

Rayner, N. A., Parker, D. E., Horton, E. B., Folland, C. K., Alexander, L. V., Rowell, D. P., et al. (2003). Global analyses of sea surface temperature, sea ice, and night marine air temperature since the late nineteenth century. *Journal of Geophysical Research*, *108*(D14). https://doi.org/10.1029/2002JD002670

Ray, P., & Zhang, C. (2010). A case study of the mechanics of extratropical influence on the initiation of the Madden-Julian Oscillation. *Journal of the Atmospheric Sciences*, *67*(2), 515–528. https://doi.org/10.1175/2009JAS3059.1

Ren, P., Kim, D., Ahn, M.-S., Kang, D., & Ren, H.-L. (2021). Intercomparison of MJO column moist static energy and water vapor budget among six modern reanalysis products. *Journal of Climate*, *34*(8), 2977–3001. https://doi.org/10.1175/JCLI-D-20-0653.1

Roundy, P. E. (2008). Analysis of convectively coupled Kelvin waves in the Indian Ocean MJO. *Journal of the Atmospheric Sciences*, *65*(4), 1342–1359. https://doi.org/10.1175/2007JAS2345.1

Roundy, P. E. (2012). The spectrum of convectively coupled kelvin waves and the Madden-Julian Oscillation in regions of low-level easterly and westerly background flow. *Journal of the Atmospheric Sciences*, *69*(7), 2107–2111. https://doi.org/10.1175/JAS-D-12-060.1

Roundy, P. E. (2014). Regression analysis of zonally narrow components of the MJO. *Journal of the Atmospheric Sciences*, *71*(11), 4253–4275. https://doi.org/10.1175/JAS-D-13-0288.1

Sardeshmukh, P. D., & Hoskins, B. J. (1988). The generation of global rotational flow by steady idealized tropical divergence. *Journal of the Atmospheric Sciences*, *45*(7), 1228–1251. https://doi.org/10.1175/1520-0469(1988)045<1228:TGOGRF>2.0.CO;2

Sentić, S., Fuchs-Stone, Ž., & Raymond, D. J. (2020). The Madden-Julian Oscillation and mean easterly winds. *Journal of Geophysical Research: Atmospheres*, *125*(10), e2019JD030869. https://doi.org/10.1029/2019JD030869

Shi, X., & Bretherton, C. S. (2014). Large-scale character of an atmosphere in rotating radiative-convective equilibrium. *Journal of Advances in Modeling Earth Systems*, *6*(3), 616–629. https://doi.org/10.1002/2014MS000342

Shi, X., Kim, D., Adames, Á. F., & Sukhatme, J. (2018). WISHE-moisture mode in an aquaplanet simulation. *Journal of Advances in Modeling Earth Systems*, *10*(10), 2393–2407. https://doi.org/10.1029/2018MS001441

Sobel, A., & Maloney, E. (2013). Moisture modes and the eastward propagation of the MJO. *Journal of the Atmospheric Sciences*, *70*(1), 187–192. https://doi.org/10.1175/JAS-D-12-0189.1

Sooraj, K. P., Kim, D., Kug, J.-S., Yeh, S.-W., Jin, F.-F., & Kang, I.-S. (2009). Effects of the low-frequency zonal wind variation on the high frequency atmospheric variability over the tropics. *Climate Dynamics*, *33*(4), 495–507. https://doi.org/10.1007/s00382-008-0483-6

Stevens, B., Satoh, M., Auger, L., Biercamp, J., Bretherton, C. S., Chen, X., et al. (2019). DYAMOND: The dynamics of the atmospheric general circulation modeled on non-hydrostatic domains. *Progress in Earth and Planetary Science*, *6*(1), 61. https://doi.org/10.1186/s40645-019-0304-z

Straub, K. H. (2013). MJO initiation in the real-time multivariate MJO index. *Journal of Climate*, *26*(4), 1130–1151. https://doi.org/10.1175/JCLI-D-12-00074.1

Straub, K. H., & Kiladis, G. N. (2002). Observations of a convectively coupled Kelvin wave in the eastern Pacific ITCZ. *Journal of the Atmospheric Sciences*, *59*, 30–53.

Straub, K. H., & Kiladis, G. N. (2003a). Extratropical forcing of convectively coupled Kelvin waves during austral winter. *Journal of the Atmospheric Sciences*, *60*, 526–543.

Straub, K. H., & Kiladis, G. N. (2003b). The observed structure of convectively coupled Kelvin waves: Comparison with simple models of coupled wave instability. *Journal of the Atmospheric Sciences*, *60*(14), 1655–1668. https://doi.org/10.1175/1520-0469(2003)060<1655:TOSOCC>2.0.CO;2

Sukhatme, J. (2014). Low-frequency modes in an equatorial shallow-water model with moisture gradients. *Quarterly Journal of the Royal Meteorological Society*, *140*(683), 1838–1846. https://doi.org/10.1002/qj.2264

Tao, W.-K., Chern, J.-D., Atlas, R., Randall, D., Khairoutdinov, M., Li, J.-L., et al. (2009). A multiscale modeling system: Developments, applications, and critical issues. *Bulletin of the American Meteorological Society*, *90*(4), 515–534. https://doi.org/10.1175/2008BAMS2542.1

Tulich, S. N. (2015). A strategy for representing the effects of convective momentum transport in multiscale models: Evaluation using a new superparameterized version of the Weather Research and Forecast model (SP-WRF). *Journal of Advances in Modeling Earth Systems*, *7*(2), 938–962. https://doi.org/10.1002/2014MS000417

Tulich, S. N., & Kiladis, G. N. (2012). Squall lines and convectively coupled gravity waves in the tropics: Why do most cloud systems propagate westward? *Journal of the Atmospheric Sciences*, *69*(10), 2995–3012. https://doi.org/10.1175/JAS-D-11-0297.1

Tulich, S. N., & Mapes, B. E. (2008). Multiscale convective wave disturbances in the tropics: Insights from a two-dimensional cloud-resolving model. *Journal of the Atmospheric Sciences*, *65*, 140–155.

Tulich, S. N., & Mapes, B. E. (2010). Transient environmental sensitivities of explicitly simulated tropical convection. *Journal of the Atmospheric Sciences*, *67*(4), 923–940. https://doi.org/10.1175/2009JAS3277.1

Tulich, S. N., Randall, D. A., & Mapes, B. E. (2007). Vertical-mode and cloud decomposition of large-scale convectively coupled gravity waves in a two-dimensional cloud-resolving model. *Journal of the Atmospheric Sciences*, *64*, 1210–1229.

Wang, B., & Chen, G. (2017). A general theoretical framework for understanding essential dynamics of Madden-Julian Oscillation. *Climate Dynamics*, *49*(7), 2309–2328. https://doi.org/10.1007/s00382-016-3448-1

Wang, L., Li, T., & Chen, L. (2019). Modulation of the Madden-Julian Oscillation on the energetics of wintertime synoptic-scale disturbances. *Climate Dynamics*, *52*(7), 4861–4871. https://doi.org/10.1007/s00382-018-4447-1

Wang, L., Li, T., & Nasuno, T. (2018). Impact of Rossby and Kelvin wave components on MJO eastward propagation. *Journal of Climate*, *31*(17), 6913–6931. https://doi.org/10.1175/JCLI-D-17-0749.1

Wedi, N. P., Polichtchouk, I., Dueben, P., Anantharaj, V. G., Bauer, P., Boussetta, S., et al. (2020). A baseline for global weather and climate simulations at 1 km resolution. *Journal of Advances in Modeling Earth Systems*, *12*(11), e2020MS002192. https://doi.org/10.1029/2020MS002192

Wheeler, M., & Kiladis, G. N. (1999). Convectively coupled equatorial waves: Analysis of clouds and temperature in the wavenumber-frequency domain. *Journal of the Atmospheric Sciences*, *56*, 374–399.

Wolding, B. O., Maloney, E. D., & Branson, M. (2016). Vertically resolved weak temperature gradient analysis of the Madden-Julian Oscillation in SP-CESM. *Journal of Advances in Modeling Earth Systems*, *8*(4), 1586–1619. https://doi.org/10.1002/2016MS000724

Xie, P., & Arkin, P. A. (1997). Global precipitation: A 17-year monthly analysis based on gauge observations, satellite estimates, and numerical model outputs. *Bulletin of the American Meteorological Society*, *78*(11), 2539–2558. https://doi.org/10.1175/1520-0477(1997)078<2539:GPAYMA>2.0.CO;2

Yang, G.-Y., Hoskins, B., & Slingo, J. (2003). Convectively coupled equatorial waves: A new methodology for identifying wave structures in observational data. *Journal of the Atmospheric Sciences*, *60*(14), 1637–1654. https://doi.org/10.1175/1520-0469(2003)060<1637:CCEWAN>2.0.CO;2

Yang, G.-Y., Hoskins, B., & Slingo, J. (2007). Convectively coupled equatorial waves. Part II: Propagation characteristics. *Journal of the Atmospheric Sciences*, *64*(10), 3424–3437. https://doi.org/10.1175/JAS4018.1

Yang, G.-Y., & Hoskins, B. J. (1996). Propagation of Rossby waves of nonzero frequency. *Journal of the Atmospheric Sciences*, *53*(16), 2365–2378. https://doi.org/10.1175/1520-0469(1996)053<2365:PORWON>2.0.CO;2

Yang, G.-Y., & Hoskins, B. J. (2016). ENSO-related variation of equatorial MRG and Rossby waves and forcing from higher latitudes. *Quarterly Journal of the Royal Meteorological Society*, *142*(699), 2488–2504. https://doi.org/10.1002/qj.2842

Zhang, C., & Dong, M. (2004). Seasonality in the Madden-Julian Oscillation. *Journal of Climate*, *17*(16), 3169–3180. https://doi.org/10.1175/1520-0442(2004)017<3169:SITMO>2.0.CO;2

Zhang, C., & Ling, J. (2012). Potential vorticity of the Madden-Julian oscillation. *Journal of the Atmospheric Sciences*, *69*(1), 65–78. https://doi.org/10.1175/JAS-D-11-081.1